
Science Requirements Document

Version 2.11

6 June 2013

for

Burning Rate Emulator (BRE): Material Burning and Extinction in Microgravity

an ACME experiment

Principal Investigator

James Quintiere, Univ. of Maryland

Co-Investigator

Peter B. Sunderland, Univ. of Maryland

Project Scientist, BRE

Paul Ferkul

Project Scientist, ACME

Dennis P. Stocker

EXECUTIVE SUMMARY

The goal of this research is to establish the burning conditions possible in a microgravity quiescent environment. The approach is to do this using a burner to emulate (BRE, Burning Rate Emulator) the burning for real condensed fuels, representative of common liquids and solids. This will be done for quasi-steady burning conditions, albeit ideal in some cases, but the BRE will range over a wide spectrum of real fuel properties. The key properties governing steady burning are (1) the heat of gasification, (2) the surface re-radiation heat flux, and (3) the heat of combustion. Flame radiation is also relevant in general and can be represented in terms of the laminar smoke point. Its importance in microgravity flames needs study, but the first three properties are key.

Currently NASA assesses the flammability hazard of materials for use in space flight by an upward flame spread “pass-fail” test (Test 1), and supplements with data from the Cone Calorimeter (Test 2). The latter test has the capability of measuring the three properties listed above. Hence, the successful application of the BRE in microgravity can enhance the usefulness of Test 2.

Fundamental and ad hoc testing in microgravity at quiescent conditions has shown that quasi-steady flames can be supported on candle-wicks, droplets, jets and, at very low ambient velocities, small plastic samples and a burner flame. The established flames tend to have spherical or semi-ellipsoidal shapes. Our preliminary work burning ethanol on planar wicks of 1×4 cm suggest similar shapes in aircraft and drop tower tests. But this work showed instabilities in the drop tower, and needs further exploration. Theoretical analysis based on microgravity jet flame length correlations suggests that a 50 mm diameter planar material could support quasi-steady combustion in microgravity for some liquid and plastic fuels. The analysis indicates that burning depends on diameter, so several additional burner sizes will be needed to examine this effect.

Gas burners like the BRE have been used to successfully simulate burning of a wide range of fuels in terms of their B numbers and configurations over a range of Grashof numbers. We have successfully shown that for planar burning at different angle orientations that a burner can emulate the flame standoff distribution, and even match the onset of unsteadiness to turbulent flow. Theoretical analyses of such a problem are limited by the inability to accurately deal with flame radiation, turbulence and variable properties. A burner simulation can be far superior as it inherently contains these effects.

The construction of a 50 mm diameter prototype BRE burner with flame heat flux sensors has enabled us to emulate both a methanol and heptane pool fire of the 50 mm diameter, reproducing its color, flame character and shape, and heat of gasification for nearly the same surface temperatures. We show that the BRE is capable of displaying the burning conditions in terms of the fuel properties of heat of combustion, heat of gasification, and surface re-radiant heat flux (with some likely effect of smoke point). A preliminary 3-D plot of steady burning gives a flammability mapping in terms of these variables under conditions of gravity and atmospheric variations. A mapping in microgravity can demonstrate the burning conditions for a wide range of real materials in terms of these properties. In addition the effect of external radiation can indirectly be assessed. The 50 mm burner has been redesigned, along with a 25 mm burner, to reduce edge effects, provide improved heat flux sensors with temperatures, and cooling water has been dropped from the both the burner and the heat flux sensors in microgravity experiments.

The primary objective is to observe the burning behavior (including extinction) in long-duration microgravity for methane/nitrogen and ethylene/nitrogen mixtures on a porous circular burner of 25 and 50 mm diameter at various pressures, ambient oxygen, and CO₂ (desired, to assess extinguishment). Ignition will not be directly studied in microgravity studies, as we believe normal-gravity experiments are sufficient for its study. Another objective is to obtain conditions that can be related to microgravity behavior of condensed fuels that embrace the scope of real liquid and solid fuels.

We think these results can establish fuel properties that directly relate to the fire hazard in spacecraft, and these properties can be derived from NASA Test 2. The BRE is an efficient, safe, and comprehensive technique for achieving these results.

This version of the Science Requirements Document has been refined since the Science Concept Review (Aug 28, 2012). The panel wrote at that time that they “strongly encourage continued development of the BRE experiment for implementation into the ACME and testing on the ISS.” We have tried to address most of their recommendations and suggestions. In addition, work has progressed to include the development of two papers, and the commencement of drop facility testing of the BRE. Those results have shown quasi-steady flames, and are very encouraging.

TABLE OF CONTENTS

1. INTRODUCTION.....	3
1.1 Goal of the study.....	3
1.2 Motivation for basing flammability in microgravity on material properties.....	3
1.3 Background of combustion in microgravity.....	5
1.4 Overview of the use of burners to emulate burning of materials.....	6
1.5 Review of supporting work for BRE.....	7
1.6 Issues for determining flammability in microgravity.....	15
2. FLIGHT EXPERIMENT.....	21
2.1 Knowledge Lacking and Knowledge to be Gained by Flight Tests.....	21
2.2 Experimental Objectives.....	22
2.3 Summary of Approach.....	22
2.4 Science Data End Products.....	22
3. EXPERIMENT REQUIREMENTS.....	25
3.1 Requirements Discussion.....	25
3.2 Operational Sequence [ISRD 4.5].....	29
3.3 Test Matrix [ISRD 5.5].....	30
3.4 Science Success Criteria [ISRD 6.5].....	30
3.5 Post Flight Data Analysis Plan.....	31
4. REFERENCES.....	32
APPENDIX 1: APPENDED PAPERS.	33

1. INTRODUCTION

1.1 Goal of the study

The goal of this study is to establish the burning conditions for materials in a quiescent microgravity environment. The burning conditions will represent those of steady burning with the heat of gasification of the material as the principal fuel property that controls such burning. In addition, the heat of combustion controlling flame extent, surface reradiation heat flux, and flame radiation properties will influence the burning rate. We seek to define the burning in terms of these properties by using an emulator having a controlled gaseous fuel supply to simulate steady burning of material with those properties. The burning rate emulator (BRE) can be operated to represent a range of real solid and liquid fuels, and considering an effective heat of gasification can also simulate an applied external heat flux.

Steady burning can be expressed as

$$\dot{m}'' = \frac{\dot{q}_f'' - \dot{q}_{rr}'' + \dot{q}_e''}{L} \quad (1)$$

where \dot{q}_f'' is the incident flame heat flux, \dot{q}_{rr}'' is the surface radiative loss heat flux to ambient, \dot{q}_e'' is the incident external radiative heat flux, and L is the heat of gasification. An effective heat of gasification can be defined as

$$L_{eff} = L + \frac{\dot{q}_{rr}'' - \dot{q}_e''}{\dot{m}''} \quad (2)$$

such that

$$\dot{m}'' = \frac{\dot{q}_f''}{L_{eff}} \quad (3)$$

The flame heat flux will be controlled by diffusive and radiative components, and the surface heat flux by the temperature of the vaporizing surface. In the case of the emulator burner (BRE), it is the surface burner temperature that gives the surface re-radiation. Heat flux gages in the surface will record the flame heat flux distribution. With the measured gas flow rate of the burner, an effective heat of gasification can be determined for all steady burning conditions according to Eq. (3). Consequently, values of L , with and without assistance from an external heat source, can be determined from Eq. (2). By varying the gaseous fuel, the heat of combustion and the radiation character (notably the smoke point) can be varied. For a given configuration, a wide range of burning conditions can be readily established with the emulator (BRE).

At first, the burner will confirm the burning of real materials in a normal gravity quiescent atmosphere. Then it will be used to establish the burning conditions in microgravity. Its advantage will be its efficiency to range through a spectrum of fuels, and its ease of operation. The feasibility of the emulator will be established in the sections to follow.

1.2 Motivation for basing flammability in microgravity on material properties

On Earth, gravity assists flow in fire to supply air and promote fire spread. For many solid and some common liquid fuels, preheating is needed to achieve burning. Materials have a critical heat flux (CHF) below which ignition is not possible. This CHF depends on the heat loss from the material on heating, and convective heat loss contributes. The convective loss is purely diffusive in microgravity, and therefore the CHF is lower. So ignition of materials in spacecraft under microgravity conditions could be somewhat easier than on Earth in a quiescent atmosphere. For comfort in a spacecraft environment there is likely to be some small ambient flow with velocities of about 6 – 20 cm/s (Ross, 2001). Such flows are known to promote spread and

burning in microgravity. But it is useful to examine, in the extreme, the conditions of burning in a purely quiescent atmosphere. Results in quiescent conditions certainly set a floor for the burning conditions. For fire safety in space it is important to know the burning conditions of a given fuel. Currently there is no way to determine these conditions. The present study seeks to express these conditions in terms of measureable material properties, and to consider the role of external heat addition, so important to fire growth on Earth.

Current flammability criteria for space flight applications are contained in documents PSS-01-721 and NHB 8060-1 (1998) as prescribed, respectively, by ESA and NASA. The documents are considered as equivalent. The Upward Flame Propagation (Test 1) is the dominant test for material flammability by NASA. It tests the flame propagation of a vertical sample $30 \times 6.4 - 7.5$ cm wide, under a small electric source heat flux of 75 kW/m^2 . The atmospheric conditions are controlled. Burn length and time are recorded. It is considered a pass-fail type test, similar to the UL-94 test, commonly used by industry for plastic components. The latter uses a premixed flame source, and samples 12.5×1.3 cm. In UL-94 the pass-fail performance could be correlated with the ratio of the heat of combustion to heat of gasification for a material (Downey, 2009).

Ohlemiller (1992) found that NASA Test 1 results for a material did not correlate with NIST flammability tests that measure ignition, burning rate, and opposed flow flame spread. He recommended that Test 1 be modified to include the addition of external radiant heating. In fact, the current NASA requirements use the Cone Calorimeter with external heat fluxes of $25 - 75 \text{ kW/m}^2$ (Test 2) to supplement information gained from Test 1. Test 1 with a “pass-fail” criteria, and even supplemental information gained from Test 2, do not explicitly give a basis for predicting performance in microgravity. Indeed, Ohlemiller recommended the study of flame spread in microgravity using a prescribed flow and heat flux. He said, “Without such information, spacecraft designers are confronted with unquantifiable risks regarding fire safety.” The FIST program with Fernandez-Pello at UC Berkeley (Ross, 2001) is the only current program aimed to examine these combined effects of radiation and flow. Nevertheless, the current NASA material compliance by flammability testing does not give information needed to predict performance in microgravity.

There is a need to establish a basis for testing flammability on Earth to extrapolate to microgravity applications. First, there is a need to establish the conditions of burning in microgravity. Secondly, it is essential to represent the condition of burning in terms of established models and material properties. The correlation of performance in UL-94 with the property ratio, heat of combustion to heat of gasification, shows a linkage to the NASA Test 1 test. Both of these properties are determinable from the NASA Test 2 test, as demonstrated by Tewarson (2002). Thirdly, as steady burning is directly related to the heat of gasification property, the establishment of quiescent burning in microgravity would provide a direct connection between a property and burning. Truly, some materials, such as those that char, do not fit this simple steady burning model, yet their burning character can still be approximately represented by a relatively high heat of gasification. For example, while wood burns unsteadily with a char, its average burning rate can be represented by an effective heat of gasification of $4 - 6 \text{ kJ/g}$. Fourthly, a burning rate emulator (BRE) can potentially display the conditions of burning in microgravity experiments. Hence the BRE can be used to assess a range of burning conditions to find a domain of burning and the properties that would allow it. Moreover, the simple burning model indicated by Eqs. (1) – (3) would allow the prediction of burning with the addition of radiant heat flux. While we do not intend to vary the external heat flux, the results of the BRE can be interpreted in terms of these relationships. The BRE can determine a range of burning

conditions in microgravity as a function of heat of gasification, reradiation heat flux, applied radiant heat flux, heat of combustion and smoke point. The latter two properties can be varied by changing the gaseous fuel supply of the BRE. In addition, nitrogen can be added to the gaseous fuel to extend a measurement range for heat of gasification.

The establishment of quasi-steady burning of materials in microgravity has not been fully established. Anecdotal tests indicate that this is possible. The special nature of burning in a purely diffusive environment must be fraught with new effects. Some of these effects have been seen among current fundamental research studies on droplets and flame spread over thin materials. Other effects involve the small entrainment ambient oxidizer due to the velocity of the vaporizing fuel, three-dimensional effects, and the propulsion of flaming droplets and brands caused by pressurization during vaporization. Also the effect of radiation feedback, so common to fire growth on Earth, has not been fully explored, and is likely to be a factor.

A serious fire accident occurred on the MIR (Ross, 2001) when a solid propellant oxygen generator ignited producing a “blowtorch-like white conical flame” that caused other materials to become involved while extinguishment was initiated by the crew. The fire burned out and caused extensive smoke damage. Hopefully, a more serious event is not waiting to happen. Yet it is likely that the “perfect storm” of conditions can be manifested to produce a serious and sustained spacecraft fire accident. The role of materials will be responsible. We should fully understand how these materials will behave, and how to relate them to Earth-bound testing.

1.3 Background of combustion in microgravity

Experiments in Skylab (Ross, 2001; Kimzey, 1974) indicated sustained burning of thin paper and plastics. More recent experiments indicate flame spread on thin paper and plastic thin cylinders in microgravity (Ross, 2001). Spread on 4.5 mm diameter rods of Delrin, PMMA and HDPE in the MIR was achieved in opposed flows down to 1 cm/s. Below that speed, the spread and burning ceased (Ross, 2001). Opposed flow spread has been well documented, and appears more favorable than concurrent spread. It is indicated that concurrent spread could be limited due to upstream vitiation by the transport of combustion products. Opposed flow spread in a quiescent atmosphere has been shown to depend on material, thickness, and oxygen concentration (Ross, 2001).

Perhaps the most striking example of quasi-steady burning has been the burning of candle flames on the MIR (Ross, 2001) for periods ranging from about 100 s to more than 45 minutes. A spherical flame formed around the wick. Attempts to repeat this in shuttle flights led to similar, but much shorter durations of burning. The MIR flights had atmospheres of 0.22 – 0.25 oxygen mole fraction, with a metal mesh screen surrounding the experiment; while the Shuttle had 0.217 oxygen fraction and a perforated plastic box enclosing the experiment (Dietrich et al., 2000). These differences in containment likely affected the input of fresh air to the candle flame and its burning duration. It was noted that the wax melt at the base of the wick distorted into a ball, and the flames oscillated before extinction.

The candle experiments clearly indicate the capability of quasi-steady sustained burning in a quiescent atmosphere of surface burning. This is also born out in droplet experiments by Kumagai and others (Ross, 2001). The droplet flame can be considered quasi-steady as the droplet diameter is reduced in burning. The droplet burning rates are slightly less than the ideal theoretical thin flame spherical solutions, but the behavior has a similar dependence with droplet diameter. Extinction occurs as the drop diameter is decreased, with diffusive effects governing small initial drops, and radiative effects for larger droplets. There are other instances of quasi-

steady diffusive flames in microgravity. Small diameter jet flames of 0.4 – 2.7 mm yielded spherical flames of durations from 150 – 300 s (Ross, 2001). Also Sunderland et al. (1999) recorded flames for port diameters up to 3.3 mm, and Reynolds (Re) from about 10 – 1700 in microgravity. Their low Re flames were spherical, and the higher Re flames elongated. An empirical relationship indicated the flame length to port diameter was linearly proportional to the Re , with the constant of proportionality depending on fuel type. The constant was about 30% higher for the non-buoyant flames, perhaps due to the lower entrainment of air.

It would appear that a spherical flame shape forms a stable quasi-steady flame for droplets, jets at low Re , and the candle with the cylindrical wick. Three-dimensional planar surfaces burning in microgravity are likely to remain stable when achieving a similar flame shape. Brahmi et al. (2005) used a gaseous burner to simulate burning in microgravity under flow conditions. They burned ethane over a 60×60 mm sintered bronze plate in oxygen-nitrogen atmospheres flowing over the plate at velocities of about 10 – 150 mm/s. They found, for 120 experiments under microgravity conditions, a mapping of fuel velocity with oxidizer velocity indicated three regions of flame shapes during burning. These regions are shown in Figure 1. The flames indicated an elliptical shape in Region I, parabolic in Region II and linear in Region III. The elliptical flames for points the (a) and (b) location of the mapping are shown in Figure 2. It is noteworthy that quasi-steady elliptical flames were produced for this planar geometry at nearly quiescent conditions ($U_\infty \sim 5$ mm/s) in microgravity. Their establishment in quiescent flow needs to be demonstrated.

Perhaps this evidence suggests a spherical-like flame can support quasi-steady diffusive burning in microgravity quiescent conditions for other configurations.

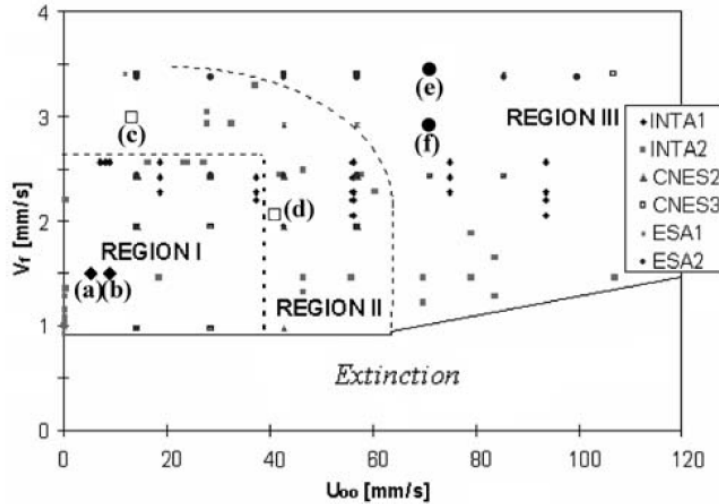


Figure 1. Regions of steady burner flames in microgravity in terms of fuel V_f and oxidizer U_∞ velocities from Brahmi et al. (2005).

1.4 Overview of the use of burners to emulate burning of materials

Orloff and deRis (1971), deRis et al. (1975) and Kim et al. (1971) pioneered the use of sintered metal burners for studying the burning of planar condensed-phase steady burning. As with the Brahmi et al. (2005) burner, the flow of the fuel is distributed uniformly over the burner. This uniform flow is in contrast to the actual flow velocity of the supplied vapor that is governed by the local heat transfer from the flame. As the flame shape changes, the vapor velocity does also.

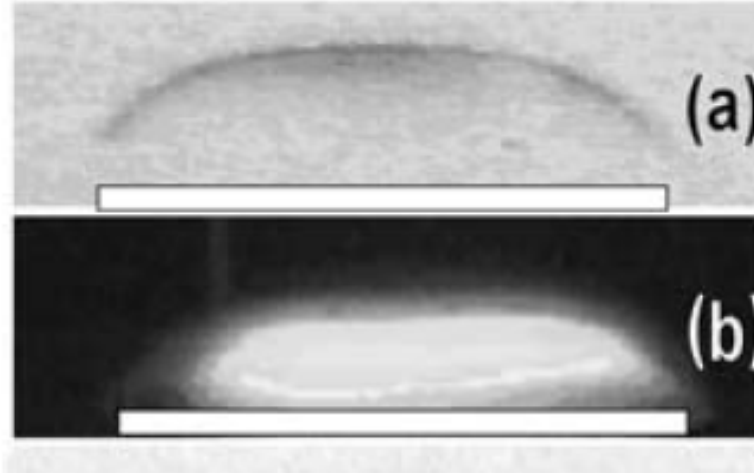


Figure 2. Elliptical flame shapes for (a) and (b) in Fig. 1a from Brahmi et al. (2005).

Yet despite this difference, deRis and co-workers successfully simulated burning conditions for a wide range of B numbers. The B number is defined as

$$B \equiv \frac{Y_{ox} \Delta h_c / r - c_p (T_v - T_\infty)}{L} \quad (4)$$

where Y_{ox} is the ambient oxygen mass fraction, Δh_c is the heat of combustion, r is the stoichiometric oxygen to fuel ratio, c_p is the specific heat of gas mixture, T_v is the surface vaporization temperature, and T_∞ is the ambient temperature.

For a given ambient condition, the B number is principally a function of the heat of gasification, L . The burning rate per unit area is also principally a function of the B number in purely diffusive or convective burning. Of course flame radiation and surface reradiation disturb this simple dependence. Yet the relatively simple dependence could be emulated by the deRis burner, and shown to follow laminar-burning theory. So despite the imperfection of a uniform burner velocity, the results yielded theoretically supported results for burning and flame shape.

In the deRis burner, the heat of gasification was determined by Eq. (1) with no external radiation and negligible reradiation. The latter was accomplished by cooling water through the burner's sintered metal matrix. An energy balance on the cooling water, after considerable time to achieve thermal equilibrium of the burner, allowed an average flame heat flux to be determined. Nitrogen addition to the gaseous fuel also allowed for variations in the supplied fuel mixture mass flux.

Because we were to follow this burner approach, we sought to establish some further support for its accuracy and to help allow us to develop a skilled approach.

1.5 Review of supporting work for BRE

We shall review our work to date, and show how it has evolved from our original objective to the current application of quiescent microgravity burning. It will display our approach, exploration of burning in microgravity, and the development of the burner concept and prototype.

1.5.1 Study of flat surface burning in microgravity

Initially this study was to consider burning in various gravity space applications, such as the Moon and Mars environments. An early consideration was to explore such conditions in aircraft

gravity simulations. Thus, a test of the burner approach was to consider the burning on a flat plate at various inclinations, with burning on top and the bottom. This work allowed us to explore this burning configuration by tests with real fuels, with a burner, and through theoretical analyses. In short, the results help to establish the credibility and accuracy of the emulation with a burner, and the limitations of theory to predict the results. A brief summary of this work follows, and Bustamante et al. (2012) presented a recent paper covering it.

For the inclined plate burning experiments, laminar burning was primarily examined. This was done using two liquid fuels, methanol and ethanol, each saturated into a porous ceramic wick plate as shown in Figure 3. The plate was oriented at angles of 0° (vertical), and $\pm 30, 60$ and 90° , with negative angles indicating burning on the bottom. Steady burning could be achieved for each of these conditions; however, for top burning in particular, at flow distances exceeding about 5 cm, the onset of unsteady instabilities occurred. This was not considered fully developed turbulence. In Figure 4, the top galley shows methanol flames for a plate length of 10 cm and at the various angles. Their color is not indicative of reality, as it was rendered to gain better clarity. The galley below shows methane flames in a burner of same dimensions at each corresponding angle and flow rate. The burner consisted of a ceramic surface with 2 mm holes. The methane flow rate was matched to the average burning rate measured in the corresponding

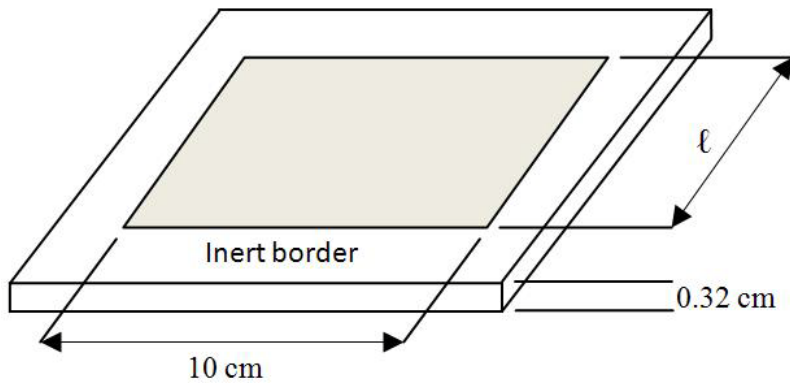


Figure 3. Porous ceramic wick substrate for liquid fuels, l ranging from 1 to 10 cm.

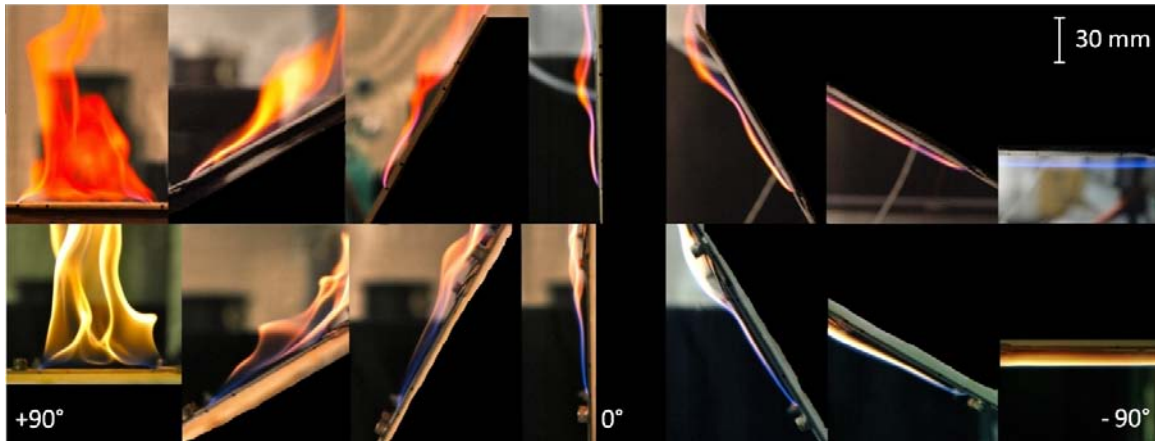


Figure 4. Methanol flames in top galley at angles $+90, 60, 30, 0, -30, -60$, and -90 . Methane flames in bottom galley at corresponding angles and burning rates.

methanol wick test of the same configuration. Images for flame standoff distances were taken within 5 – 15 s of ignition to minimize the temperature rise of the surface. The surface temperature of the burner yielded a maximum reading of 175 °C over this time period. This temperature range is higher than the boiling point of methanol, but still gives a relatively small reradiation loss compared to the flame heat flux.

A better comparison of the flame standoff position between the methanol and the methane burner is shown in Figure 5 in which two instantaneous traces were made of each. Their similarity, even in the transition instabilities, is a measure of the accuracy of the burner in simulating the methanol flames. Notably there are some differences, in particular at +30 and 0° where the onset of the transition occurred early in the methanol flame. The onset of transition appears to have had an upstream thickening effect on the standoff position. The reason for the difference at -90° is unclear.

Nevertheless, the ability of the burner to emulate the distributive aspects of the burning by these flame standoff comparisons is encouraging. It is noteworthy that theoretical analyses to achieve similar results are limited by the effects of transition instabilities, variable properties, and flame radiation. Even a DNS simulation (Raghavan et al., 2010) of this inclined plate burning was confined to considering only a 1 cm long plate. Hence, a practical way to emulate burning is using a burner, as it automatically accounts for the effects of instabilities, radiation, and property variations.

We have explored the ability to measure the total heat flux to the burning surface of the wick fuels. The heat flux was measured for the 10 x 10 cm methanol soaked wicks with a 3 mm diameter thermopile sensor (Medtherm Schmidt-Boelter heat flux transducer) located at the center of the plate. This sensor requires cooling to maintain its back-face temperature. Initial cooling with normal ambient water gave erratic results, most likely due to condensation on the sensor. This was eliminated by using water supplied at temperatures above 65 °C, the dew point

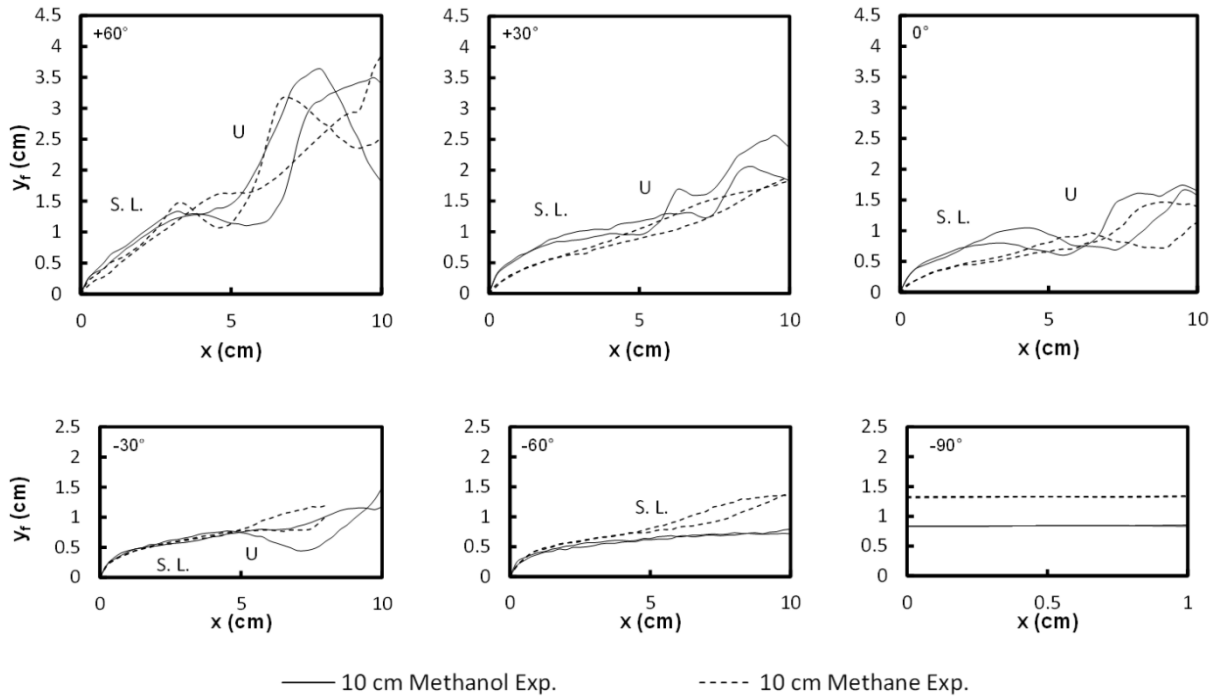


Figure 5. Trace renditions of the flame standoff position for the burner and methanol.

of most fuels associated with a diffusion flame. Figure 6 shows the measured heat flux at the center of the 10 x 10 cm Methanol wick along with the corresponding average burning flux. If laminar burning persisted over the plate, the average heat flux could be estimated from the local value at the center (5 cm). Since a transition to turbulence occurs for all angles except -90°, a simple estimation is not possible. However, for -90° where laminar conditions prevailed and the flame shape is nearly invariant from Figure 4, the flame flux measured could be taken as constant over the plate. Taking a small re-radiation into account the heat of gasification can be computed for the -90° case as $(17.3-0.3) \text{ kW/m}^2 / 11 \text{ g/m}^2\text{s} = 1.55 \text{ kJ/g}$ for methanol; actually it is 1.23 kJ/g. While this computation is approximate, it gives some confidence level that the mass and heat flux measurements are in accord. Further, it gives a good basis for incorporating such a heat flux measurement into the BRE burner.

An MS thesis has been completed on this work. A paper is to be presented at the Proc. of the Seventh International Seminar on Fire and Explosion Hazards in May 2013, and a journal paper has been submitted. That paper is appended herein. It includes additional data and theoretical results that aid in generalizing the results. This work provided us with a basis of using a burner to emulate the burning rate on flat plates of various orientations.

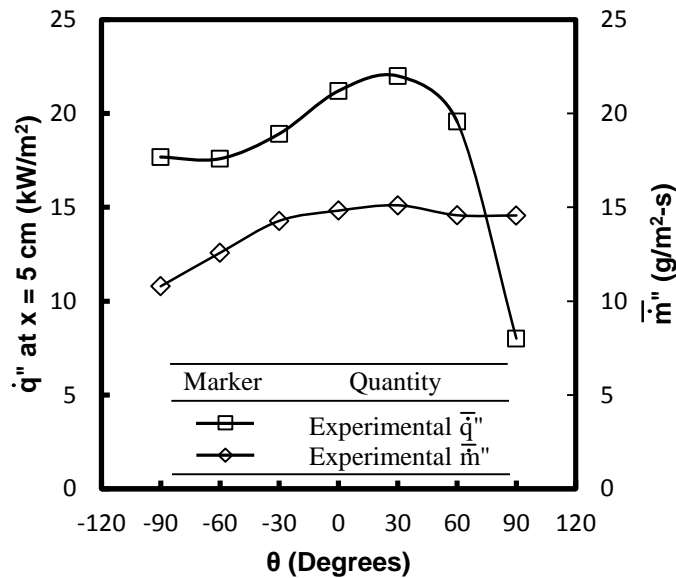


Figure 6. Average mass burning flux and center heat flux for methanol at all angles.

1.5.2 Preliminary results in microgravity

In addition to the normal gravity wick burning experiment, several microgravity experiments were made. These were performed in the NASA Glenn 5-second drop facility, and in aircraft simulations of microgravity. These involved a wick 10 x 40 mm in size. In two drop-facility experiments at NASA Glenn, a blue ellipsoidal flame was established; then appeared unstable and extinguished during the 5 s drop. A photograph is shown in Figure 7. It was speculated that the instability may have been related to the wick placement as too close to the chamber wall.



Figure 7. Ethanol flame in microgravity drop tower experiment before extinction (40 mm length).



Figure 8. Steady flame on ethanol wick in aircraft μ -g test (40 mm length).



Figure 9. Heptane on 50 mm diameter wick, NASA Glenn drop-tower at 30 % O₂, 2 atm

Also, ethanol flames on the same size wick were used in aircraft simulations of microgravity. We recognize that this simulation for microgravity will be less satisfactory than the drop tower environment of microgravity. In the 14-microgravity aircraft experiments, a quasi-steady flame persisted the duration of the burn ranging from 6 – 20 seconds. The flames were mostly ignited in the “zero-g” period. A representative photograph of a quasi-steady flame in the aircraft is shown in Figure 8. It closely resembles the flame in Figure 7. The flame in the aircraft

microgravity test appears flatter than the one in the drop tower. The video recording in the aircraft, from which this photograph was cut, was handicapped. The video camera mounted in the rig malfunctioned, and a hand-held camera was used looking through the chamber window.

Additional NASA Glenn drop facility testing (June 19-22, 2012) used a circular flat ethanol wick of 22 and 50 mm diameter. For a normal atmosphere, the 50 mm diameter ethanol flame behaved similarly to the rectangular strip configuration of Figure 7. However, for the 22 mm diameter wick, the flame appeared to lift on the left, but sustained through the 5 s drop. In addition, a heptane flame in 30 % oxygen and 2 atm sustained almost quasi-steady burning for the full 5 s drop period. This is illustrated in Figure 9.

In November 2012, experiments were performed with a 28 mm diameter burner using methane and ethylene in the NASA 2 s drop facility. The results are reported by Takahashi et al., (2013). They find that hemispherical flames were formed and appeared to increase in size except for low flow rates. They also found the flames appeared to be more stable if the burner was heated. This burner did not have heat flux sensors to measure the thermal feedback from the flame.

Encouraged by these tests, the BRE 50 mm burner was used in the NASA 5 s drop facility commencing in February 2013. The burner surface temperatures were also recorded, but the face temperature of the thermopile heat flux gages were allowed to achieve their equilibrium; they were not measured or controlled by 65°C water as in ground tests. The tests produced quasi-steady flames for ethylene, but had difficulties with methane. Some of this type of difference of stability and ignitability was also found by Takahashi et al (2013). Hemispherical flames were found for the ethylene, and those results are summarized in Table 1. It is interesting to observe that the heat of gasification, corresponding to the burner temperature and heat flux, drops as the burning flux increases. This trend is shown more clearly in Fig. 10.

The results in Fig. 10 suggest that fires of 50 mm in diameter with liquid fuels having typical L values of about 1 kJ/g or less and some plastic materials having high heats of combustion are likely to sustain microgravity burning. However, the burning of such solids can be problematic in microgravity as relatively long times will be necessary for ignition and to achieve quasi-steady burning.

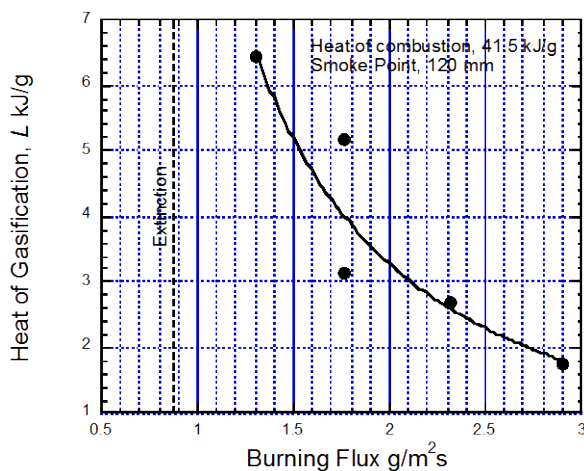


Figure 10. Heats of gasification at quasi-steady μ g burning

Table 1. Summary of 5 s drop facility burning conditions at the end of the drop

Test No.	D9023	D9024 (Extinguished)	D9027	D9028	D9029	D9030
Fuel	C ₂ H ₄	C ₂ H ₄	C ₂ H ₄	C ₂ H ₄	C ₂ H ₄	C ₂ H ₄
Ht. of comb. (kJ/g)	41.5	41.5	41.5	41.5	41.5	41.5
Smoke Point (mm)	120	120	120	120	120	120
Ignition	1g	1g	μg	μg	μg	μg
Fuel Rate (ccm)	180	90	180	135	240	300
Burning Rate (g/m ² -s)	1.76	0.88	1.76	1.3	2.32	2.9
HF_Center (kW/m ²)	5.68		5.68	5.68	4.27	3.6
HF_Edge (kW/m ²)	7.08		10	9.19	6.8	5.65
Average HF (kW/m ²)	6.85		9.29	8.61	6.38	5.31
Center T_s (°C)	133		60	66	52	48
Outer T_s (°C)	150		55	60	56	54
Averaged T_s (°C)	147.20		55.83	60.99	55.34	53.01
L (kJ/g)	3.15		5.16	6.43	2.67	1.77
Re-radiation (kW/m ²)	1.31		0.20	0.25	0.20	0.18

The result using pure methane as a fuel have not produced stable flame as yet, and the work is continuing. The heat of combustion of methane is a bit higher than the ethylene, but their wide difference in smoke point is dramatic. It is suggested that the higher soot radiation tendency of the ethylene might explain its ease in more stable burning over methane. This difference is key to further understanding these flames, and the suggest by the Review Panel to include a flame radiation measurement is proving prophetic.

It should be point out that these drop facility tests were performed with no cooling water to the burner that would control its surface temperature, and no cooling water to the two heat flux sensors. Temperature measurements of the surface indicated appropriate levels. The heat flux gages also did not have temperature-measuring capability for the sensor, but new sensors will have this ability. These tests suggest that there is no need for water-cooling of the burner or the heat flux sensors. We are continuing laboratory experiments to fully appreciate this mode of operation. The ACME cannot accommodate water-cooling loops, so this operation is essential for the BRE ISS experiments. We are still analyzing all the burner testing in the drop facilities, and will try to generalized these results in the future.

1.5.3 Burner design and validation in normal gravity

A BRE burner prototype has been designed and constructed. Its size has been selected based on our flight and drop tower tests, and the burner size used by Brahmi et al. The prototype BRE burner was selected to have an operating face of 50 mm in diameter. Due to the anticipated heat flux variation over the surface while burning in microgravity or normal gravity, two sensors are used. An appropriate averaging of the two heat fluxes should provide the needed average heat flux for computing the heat of gasification. Experiments using three heat flux sensors have evaluated several averaging techniques for two sensors to assess accuracy. The surface burner temperatures need to be measured at similar radii position to the heat flux sensors. Newly acquired heat flux sensors allow for directly measuring the sensor temperature. This is now essential as we will not monitor or use cooling water to the sensors. The burner design is discussed further in Section 3. We will accept the temperatures we get with the burner, as we

expect continued operation to approach the range of real fuel temperatures, roughly 50 – 500 °C. As a flame persists on the burner it will increase the surface temperature, thus we obtain data over a range of thermal feedback conditions.

We have tested the 50 mm BRE prototype to see if it could emulate a pool of methanol steadily burning. The mass loss rate of methanol was measured and the flame was photographed. To match the methanol with the BRE we would need to use a fuel gas with the same flow rate. Also to match the flame height and the consequently the heat flux, the fuel must have the same heat of combustion. In addition a consideration of the soot tendency was made that led to methane as the gaseous fuel. However, nitrogen must be added to the fuel stream to make the resulting fuel mixture have a heat of combustion to match that of methanol, 19.1 kJ/g (Tewarson). The gas burner BRE used a fuel mixture of 52% (volume) methane with 48% nitrogen to achieve the needed heat of combustion. The flow rate of the mixture was 33 cc/s flow rate to match the measure steady burning rate of the methanol of 11g/m²-s.

If the BRE concept is correct, the two flames should be nearly identical in appearance, and provide the same heat flux distribution. The measured heat flux in the BRE is 5.5 kW/m² for the heat flux gage located at the center, and is 21.3 kW/m² for the other gage located at 1.5 cm from the center. A weighted average over their area segments gives an average value of 15.6 kW/m². Corresponding surface temperature measurements over these respective area segments gave an average temperature of 160 °C (141 – 170 °C). Assuming an emissivity for the oxidized porous brass surface of 1, the re-radiative heat flux is 2 kW/m². Consequently, the heat of gasification associated with the BRE is computed from Eq. (1) as $L = (15.6 - 2 \text{ kW/m}^2) / (11\text{g/m}^2\text{-s}) = 1.24 \text{ kJ/g}$. The literature value for methanol is 1.20 kJ/g (Quintiere 2006). The slight mismatch is the surface temperature of the BRE compared to the boiling point of methanol at 64 °C. The visual confirmation of the BRE to emulate the methanol pool fire at 50 mm diameter is shown in Figures 11 (a) and (b) in which the flames are compared when the slightly oscillating images are similar.

We wanted to show that the burner could emulate other burning conditions. We considered a 50 mm diameter burning pool of heptane. Ethylene was selected to use as the burner gas. The heat of combustion of ethylene is very close to that of heptane, which is 41.5 kJ/g compared to 41.2 kJ/g (Tewarson), as well as the smoke point, which is 120 mm compared to 139 mm (Li and Sunderland, 2012). The gas burner BRE used pure ethylene with 26.5 cc/s flow rate to match the measured steady burning rate of the heptane of 15 g/m²-s. The measured heat flux in the BRE was 7.64 kW/m² for the heat flux gage located at the center, and is 12.74 kW/m² for the other gage located at 1.5 cm from the center. A weighted average over their area segments gives an average value of 10.9 kW/m². Corresponding surface temperature measurements over these respective area segments gave an average temperature of 211 °C (160 – 240 °C). Assuming an emissivity for the oxidized porous brass surface of 1, the reradiative heat flux is 3.12 kW/m². Consequently, the heat of gasification associated with the BRE is $L = (10.9 - 3.12 \text{ kW/m}^2) / 15.34 \text{ g/m}^2\text{-s} = 0.507 \text{ kJ/g}$. The literature value for heptane is 0.48 kJ/g (Quintiere 2006). A visual confirmation for the nature of these turbulent flames is shown in Figure 12. They are remarkably similar.

In summary of the development work, a burner is suitable for emulating the burning conditions of real materials. It has advantages over computational approaches, as it embodies variable properties, radiation, and chemical kinetics naturally within a simulation. The burning of a condensed phase liquid fuel in a planar geometry produced ellipsoidal flames in microgravity environments, but the drop tower flames became unstable and extinguished after several seconds

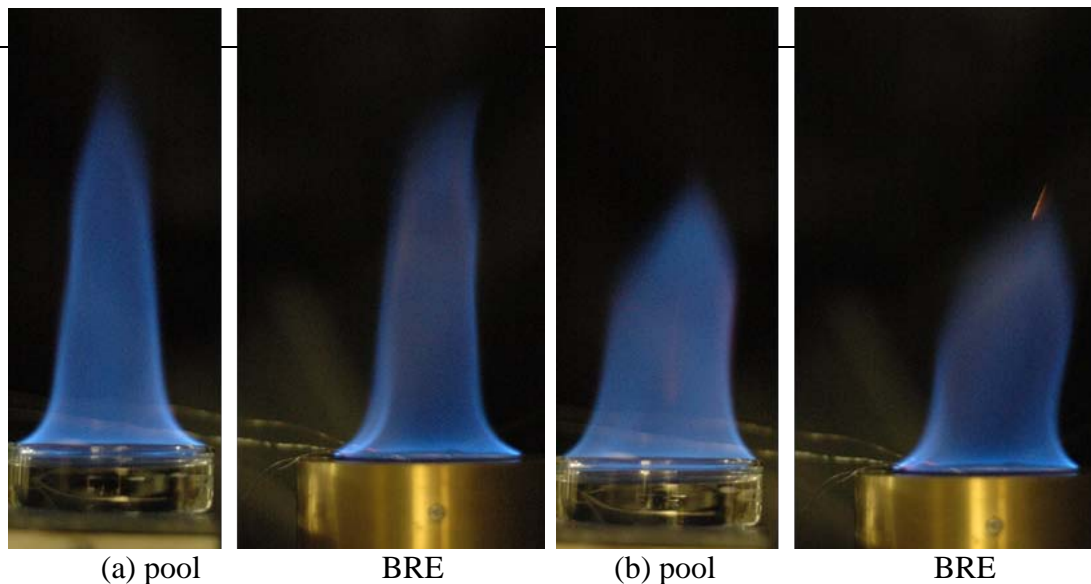


Figure 11. Comparison of 50 mm diameter methanol flame reproduced by the BRE burner.

while the aircraft flames remained quasi-steady for 20 s or more. It is suggested that fuels with the properties of ethanol may achieve quasi-steady burning in microgravity. The BRE burner did a remarkable job at reproducing a methanol flame for the same diameter pool in normal gravity. This successful reproduction lays a foundation for establish proof of the BRE concept. More extensive tests with the BRE burner in normal and microgravity can reveal the burning domain for a range of real materials, including ignition and extinction determinations. Such testing can map out a range of fuel properties that would support burning.

We have begun to test a 25 mm burner in a similar way, and found some initial difficulties. The heat flux levels over the smaller burner, operating in a laminar range gave high and varied values across the burner. The size of the heat flux sensors (1/8th inch, or about 3 mm) was believed to have been too large for the 25 mm diameter burner. We are acquiring 1/16th inch sensors. We believe the new sensors and better data for the burning of methanol at 25 mm will establish the credibility of the smaller burner in emulating real fuels on Earth. The Science Concept Review Panel believed that a smaller burner would be better for microgravity experiments. Our recent drop tower tests with the 50 mm burner appears to suggest its size is adequate, but we plan to proceed with the use the two size burners. A paper for the US Combustion Meeting in May 2013, entitled “A Burning Rate Emulator for Study in Microgravity” by Y. Zhang, M.J. Bustamante, P.B. Sunderland, J.G. Quintiere and P. Ferkul, summarizes our progress in establishing the credibility of the BRE concept and its effect use in microgravity. This paper is appended to more completely show our progress with the BRE.

1.6 Issues for determining flammability in microgravity

It is interesting to examine the prospect of burning in microgravity. A theoretical analysis can be put forth based on the relationship for steady burning, and its ability to exceed a critical flame temperature to have the flame survive. A critical temperature needed for the survival of a diffusion flame can be taken as 1300 °C (Quintiere and Rangwala, 2004). This temperature is a reasonable criterion for extinction of a laminar flame under its environmental conditions, including gravity effects. Following Eqns. (1) and (4), treating heat flux from the flame explicitly, and considering small B number as would occur near extinction, we write:

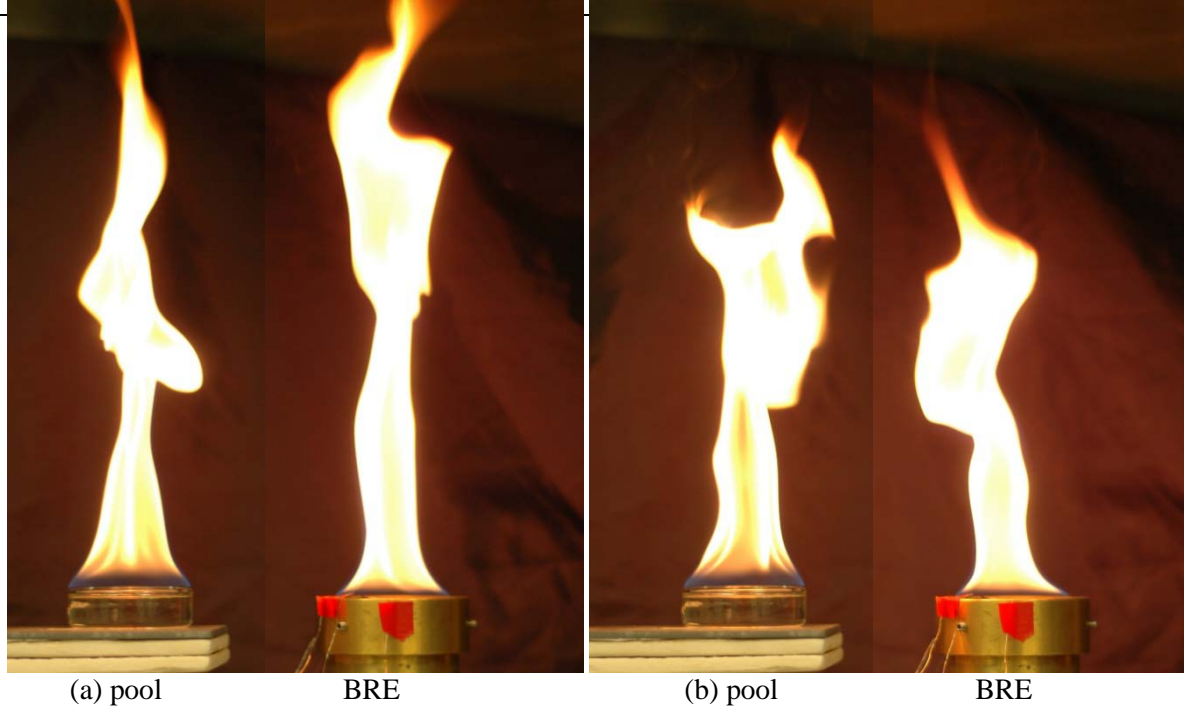


Figure 12. Comparison of 50 mm diameter heptane flame reproduced by the BRE burner.

$$\dot{m}'' L_m = \frac{h_c}{c_p} \left[Y_{ox} (1 - X_r) \Delta h_c / r - c_p (T_v - T_\infty) \right] \quad (5)$$

$$L_m \equiv L - \frac{\dot{q}_{f,r}'' + \dot{q}_e'' - \dot{q}_{rr}''}{\dot{m}''} \quad (6)$$

where L_m is an effective heat of gasification, h_c is the convective heat transfer coefficient, and X_r is the flame radiation loss fraction. The Review Panel was concerned about the change in the oxygen concentration in the microgravity test chamber for ACME. Apparently it is not continuously measured. As the B number clearly shows that the burning rate is dependent on oxygen, it is important to have this ambient value during any ISS testing.

The flame temperature (T_f) can be determined by (Quintiere, 2006):

$$c_p (T_f - T_\infty) = \frac{Y_{F,o} (1 - X_r) \Delta h_c - L_m + c_p (T_v - T_\infty)}{1 + r Y_{F,o} / Y_{ox}}. \quad (7)$$

These equations, (5), (6) and (7), can be combined by eliminating L_m to yield:

$$\dot{m}'' \Delta h_c = \frac{\frac{h_c}{c_p} \left[(1 - X_r) \Delta h_\infty - c_p (T_v - T_\infty) \right]}{Y_{F,o} (1 - X_r) + \frac{c_p (T_v - T_\infty) Y_{ox}}{\Delta h_\infty} - \frac{c_p (T_f - T_\infty)}{\Delta h_\infty} \left(\frac{Y_{ox}}{r} + Y_{F,o} \right)} \quad (8)$$

where Δh_∞ is the heat of combustion per unit ambient oxidizer, $\frac{Y_{ox} \Delta h_c}{r}$. To simplify, the following approximations are made for a pure fuel ($Y_{F,o} = 1$):

$$\begin{aligned}
\Delta h_\infty &\approx 3 \text{ kJ/g for ambient air,} \\
\frac{Y_{ox}}{r} &\approx 0.1 \text{ to } 0.3, \\
\frac{c_p(T_v - T_\infty)}{\Delta h_\infty} &\approx 0.1, \\
\frac{c_p(T_f - T_\infty)}{\Delta h_\infty} &\approx 0.4, \text{ at extinction.}
\end{aligned}$$

This allows Eq. (8) to be approximately represented at extinction as

$$\dot{m}''_{crit} \Delta h_c \approx \frac{\frac{h_c}{c_p} [(1 - X_r) \Delta h_\infty - c_p (T_v - T_\infty)]}{0.5} \quad (9)$$

Combining Eq. (9) with Eq. (5) at extinction, and recognizing that flame radiation will be small at extinction, a criterion for steady burning is established as

$$\dot{m}''_{crit} = \frac{\dot{q}''_{rr} - \dot{q}''_e}{(\Delta h_c / 2) - L}. \quad (10)$$

Materials cannot have burning rates below this critical value. Note that the addition of external radiant heating will reduce the critical burning flux. Note also that this estimate does not depend on diffusive heating, although flame radiation has been omitted.

Let us ignore the addition of external radiation, and estimate what materials are likely to burn in microgravity. As would be difficult to estimate, flame radiation is neglected here, and likely to be small in microgravity. Consequently, we apply Eq. (5) ignoring the small heat capacity term, as

$$\dot{m}'' L \approx \frac{h_c}{c_p} \Delta h_\infty - \dot{q}''_{rr}. \quad (11)$$

The convective heat transfer coefficient must be estimated for microgravity. We treat this as pure conduction, from a flame whose standoff distance is estimated from the low Re jet study of Sunderland et al. We choose a coefficient corresponding to methane, $C_f = 0.192$, and a diameter corresponding to our prototype burner, $d = 50$ mm. In terms of the burning flux the flame standoff is given as

$$\delta = \frac{C_f d^2 \dot{m}''}{\mu} \quad (12)$$

where μ is the fuel viscosity. The convective coefficient is given as

$$h_c \approx \frac{k}{\delta} \quad (13)$$

where k is the conductivity of the fuel. The following property selections are made:

$$\begin{aligned}
k &= 0.0257 \text{ W/m-K} \\
\mu &= \nu \rho = (15 \times 10^{-6} \text{ m}^2/\text{s}) (1.2 \text{ kg/m}^3) \\
c_p &= 1.0 \text{ kJ/kg-K} \\
&\text{and}
\end{aligned}$$

$d = 50 \text{ mm}$.

Consequently $\frac{h_c}{c_p} \approx \frac{1 \cdot (\text{g/m}^2/\text{s})^2}{\dot{m}''}$. Equation (10) now becomes

$$\dot{m}''^2 L + \dot{q}_r'' \dot{m}'' - \Delta h_\infty \approx 0 . \quad (14)$$

So Eq. (14) estimates the burning flux for a planar material of diameter 50 mm burning in microgravity. Larger sizes reduce the convective coefficient by $1/d^2$, and lower the burning flux. Equation (10) gives the critical flux, below which, burning cannot occur for a material.

This analysis suggests that the estimated burning flux decreases with diameter. So as the surface diameter increases, there is less chance of unassisted quasi-steady burning in microgravity. This has implications on the BRE size that we employ.

Let us select representative properties for liquid fuels, thermoplastics, high temperature polymers, and halogenated polymer. Table 2 gives generic properties, the results of computing the mass flux estimated for burning in microgravity, and the critical mass flux. It is seen from the table that generic liquid fuels would burn in microgravity, while ordinary polymers are marginal and high temperature and halogenated polymers would not burn. Of course the addition of external radiation would mitigate, and allow all to burn. It is interesting to re-examine Figure 10 that shows for heat of combustion of 41.5 kJ/g, that quasi-steady burning was achieved for a heat of gasification of about 1.8 to 6 kJ/g with a burning flux of about 2.9 to 1.3 g/m²s, respectively. With respect to Table 1, this microgravity burning is consistent with high heat of combustion liquids and thermoplastics.

This analysis has been put forward to emphasize and demonstrate the role of material properties for burning in microgravity. While it can be challenged that the heat of gasification is an approximate property for char formers, it is precise for liquids and reasonable for many thermoplastics. The BRE will operate on the basis of the heat of gasification. As Table 1 confirms the capability of generic liquids to burn, it is noteworthy that ethanol on a 10 x 40 mm wick did apparently support quasi-steady burning in the aircraft microgravity environment. Perhaps this lends data to support the overall analysis. It is the program of the BRE that will help to establish the more complete data for Table 2. The BRE result would be more reliable, and allow the effect of flame radiation to be felt and varied by changing the gaseous fuel smoke points.

Hence the BRE should be able to establish a flammability mapping in terms of heat of combustion, heat of gasification, re-radiation heat flux, and smoke point. It will give the burning flux for a given fuel for a specific burner diameter, establish extinction limits, and also establish the minimum flux for piloted ignition. These results can be established in normal gravity as well as microgravity. To illustrate how this might work we will show some preliminary results for the

Table 2. Estimated burning conditions in microgravity for a planar material of 50 mm diameter.

Parameter	Liquids	Thermoplastics	High-temperature Polymer	Halogenated Polymer
Heat of Combustion, kJ/g	30	30	15	8
Heat of Gasification, kJ/g	0.5	3	5	3
Re-radiation Flux, kW/m ²	0.5	10	20	30
Burning Flux, g/m ² s	2	0.5	0.1	0.2
Critical burn flux, g/m ² s	0.03	0.8	8	29

prototype BRE burner at 50 mm operating in normal gravity and air with pure methane and ethylene as the fuels.

A three-dimensional plot is shown in Figure 13. The axes are the heat of combustion, the heat of gasification, and the reradiation surface heat flux. Along with the smoke point, these parameters represent a set of distinct fuel properties that characterize steady burning of a material – liquid or solid. The curves for methane and ethylene were established by varying the gas flow rate from ignition to increasing values, then decreasing the flow until extinction is reached. The extinction limit is indicated on the graph. The critical mass flux for ignition and extinction are so determined, and the heat of combustion, gasification and reradiative heat flux define the material at these corresponding points. Furthermore, the plots for methane and ethylene correspond to a set the fuel properties. Each point on the lines represents a distinct solid or liquid fuel. Of course those points may not all fit a real fuel.

In addition, some real fuel data are plotted in Figure 13, including the methanol and heptane that were simulated in Figures 11 and 12. The values recorded for these fuels are displayed in Table 3. Future work will try to emulate in normal gravity some of the solid fuels listed. A full exploration of the BRE can map the flammability range for the properties: heat of combustion, heat of gasification, and re-radiation heat flux in which burning is sustained from ignition to extinction. It is noteworthy that NASA Test 2 is capable of measuring these properties of materials evaluated for space flight. We expect the smoke point, as it controls flame radiation to also have a bearing more so in normal gravity.

We intend to explore the range burning that holds in normal gravity for the three parameters: Δh_c , L and q_{rr} without any additional external heat flux. Of course, the smoke point would be a fourth parameter for consideration. The mapping can be done by operating the BRE with different gaseous fuels, including dilution with nitrogen. Valuable information on the conditions for ignition and extinction can be obtained as well, and their accuracy is superior to

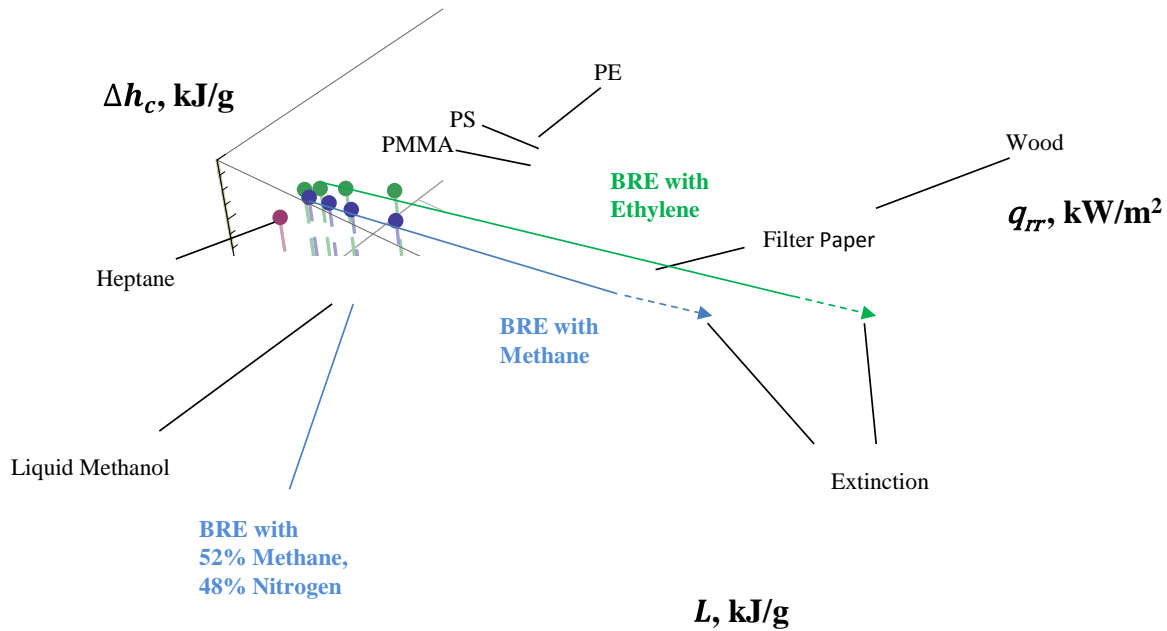


Figure 13. Flammability map of material properties.

unsteady mass loss measurements of real solid and liquid fuels. It would be interesting to test the theoretical extinction condition governed by Eq. (10). Data for real materials that fall outside of the BRE flammability range would not allow for steady burning without the assistance of additional heat flux. It is possible to use Eq. (2) to determine the needed external heat flux to afford steady burning for these materials outside of the flammability range. In this way we can test the BRE in normal gravity, and extend it to microgravity as well as examine the effects of atmospheric concentrations and pressure. In short, the BRE is an efficient way to assess burning under a variety of environmental conditions. Its exploration in microgravity can give valuable insight into material flammability in space flight.

Table 3. Approximate Properties

		Δh_c , kJ/g	L , kJ/g	q_{rr} , kW/m ²
Realistic Materials	Heptane	41.4	0.5	1
	PE	30.8	1.5	12
	PMMA	24.2	1.6	11
	PS	27	1.5	12
	Filter Paper	15	3.6	10
	Wood	12.5	5	18
	Liquid Methanol	19.1	1.2	1
BRE Simulation	Methane	50	0.85	1.47
		50	1.09	1.65
		50	1.37	1.81
		50	1.88	2.24
		50	3.04	2.63
		50	4.43	3.41
	52% Methane 48% Nitrogen	19	1.22	2
	Ethylene	41.5	0.37	2.74
		41.5	0.51	3.12
		41.5	0.74	3.67
		41.5	1.21	4.60
		41.5	1.93	5.69
		41.5	2.74	5.81
		41.5	3.89	6.95
		41.5	5.75	7.78

2. FLIGHT EXPERIMENT

2.1 Knowledge Lacking and Knowledge to be Gained by Flight Tests

Currently material selection for spacecraft is based on NASA Test 1 conducted in normal gravity. There is no scientific basis to extrapolate this test result to flammability performance in a spacecraft environment. The inherent material properties that control flammability should not change as the gravity field changes. It is known that forced convection can allow steady burning and its inclusion in microgravity only extends our current knowledge. However, quiescent burning on flat surfaces has been weakly explored in microgravity and is not predictable. There is a lack of empirical or theoretical methods for prediction based on material properties that govern steady burning. Indeed, the establishment of truly steady burning in microgravity has yet to be achieved. Even apparent steady burning is short lived in drop experiments, and might more aptly be dubbed “quasi-steady”. For now we shall use the terminology of “steady burning” without distinction, but the reader should be aware that it is ideal.

The entire concept of the BRE is to identify the regime of quasi-steady burning in microgravity as a function of materials properties. It may be so that steady burning is never achieved, and only slowly changing unsteady flames are noted. Only the available duration of flight tests will establish what is possible. In any case, Earth-based short duration microgravity experiments have not been sufficient to establish the certainty of steady flames with the BRE. In microgravity, droplet flames exhibit quasi-steady burning as the droplet shrinks. This is a diffusive extinction at small droplet diameter; also there is a radiative extinction for large drops. The latter could lead to cool quasi-steady flames. For jet flames in microgravity, quasi-steady flames have been observed but for much smaller diameters than the BRE burners. Any extrapolation from these flight experiments to the possibility of BRE quasi-steady flames is speculative. However, recent 5 s drop experiments with ethylene in the 50 mm BRE burner indicate slow sustained flame growth at the end of the test, and the prospect of a steady flame. Below a critical flow rate, the flame could not be sustained, indicating a diffusive extinction limit. Extinction at a larger flow rate, indicative of droplet radiative extinction, was not explored. In short, we will not know how the BRE flames will behave until adequate flight duration tests are done. Mathematical modeling will hopefully give us some guidance, but this phase of the project has not begun yet.

The proposed tests aboard the ISS aims to establish the range of quasi-steady burning conditions for condensed fuels in microgravity. We will identify the associated material properties and the real materials that are represented. Once established based on fuel properties, NASA Test 2 could be used as a basis for establishing comparable properties for real materials. This is possible as NASA Test 2 has the ability to measure the heat of combustion, heat of gasification and burning surface temperature. Only the smoke point would remain, and this too is possible. Then the four properties characterizing the flammability map would define conditions of burning in microgravity. This could elevate the role of NASA Test 2 over Test 1. This would close the loop for the use of ground-based tests to assess the true flammability of materials in microgravity.

The BRE mapping of material flammability in microgravity would provide a scientific rationale for assessing the fire hazard. We intend to explore the range of heats of combustion from about 5 – 50 kJ/g, and heats of gasification from about 0.5 – 5 kJ/g. These properties embrace common materials including paper, plastics and liquids. In addition, the BRE concept could be exploited in follow-on tests concerned with flowing ambients and extinguishing agents.

2.2 Experimental Objectives

The BRE flight program seeks to establish the burning conditions in a quiescent microgravity ambient in terms of material properties. The specific flight objectives are as follows.

1. Observe burning behavior in long-duration microgravity for CH_4/N_2 and $\text{C}_2\text{H}_4/\text{N}_2$ mixtures on porous circular burners of 25 and 50 mm diameter. Consider O_2/N_2 ambients with various pressures and ambient O_2 concentrations and pressures. NASA-considered atmosphere for human space missions will be examined: 14.7 psia, 21 % oxygen; 10.2 psia, 26.5 %; and 8.2 psia, 34 % oxygen. Emphasize fuel conditions that can be related to a diverse range of condensed fuels.
2. Consider the conditions of Objective 1 for ambients of O_2/CO_2 (desired).
3. Consider the conditions of Objectives 1 – 2 for extinction limits.

2.3 Summary of Approach

To accomplish the above objectives, flight experiments are proposed. Additionally, preliminary flight tests will be performed to verify the experiment operations and for comparison with ground-based tests.

For each test, conditions will be established for the chamber contents, namely choice of diluent, oxygen concentration, and pressure. Fuel flow will commence followed by ignition. The flames will initially be observed without varying the fuel flow rate. Because burner surface temperature and heat flux will vary, this will allow a broad range of conditions to be observed during a single test. As the surface temperature of the burner increases, and the flame remains steady, a continuous set of data is produced for the flammability map. Eventually either the flame will extinguish, the surface temperature of the burner will equilibrate, or the temperature limit of the heat flux sensor will be reached. At this time the fuel flow will be terminated. So a test should terminate for a given flow rate at extinction, and for continued burning when the burner surface temperature has steadied or the temperature limit of the heat flux sensor is neared.

The extinction limit could be found once the burner temperature has steadied, and the heat flux sensor has not exceeded its limit. At that state, the flow rate can be reduced in small increments, until extinction is observed and the flow rate shut off. Again, in this process, new data is being produced for the flammability map.

Ignition limit tests are not proposed for microgravity, but we will explore these under normal gravity. We believe there is better control on Earth-based ignition testing and that these results should carry over to microgravity conditions.

In addition to the flight experiments, in normal gravity testing will continue. These tests will involve gaseous, liquid, and solid fuels. These experiments will further establish the validation of the BRE for 1-g applications and show its usefulness to establish 1-g ignition and extinction limits. As available, drop facility testing will be used to refine procedures, test instrumentation, and help to establish viable flow conditions.

We will also pursue a CFD model for the quiescent microgravity burning. This will also guide us in the flight experiments, and potentially provide a predictive methodology.

2.4 Science Data End Products

The science data end products (SDEP) are the tables, figures, and analyses that will be reported in the archival literature (not the raw data from the experiment). Table 4 indicates the planned SDEP according to the BRE objectives. The science requirements and the experiment success criteria (see below) are developed from this list of SDEP. The principal delivery would be a

complete flammability mapping to indicate burning in microgravity. This would include extinction limits and effect of radiation through the smoke point. Perhaps a successful CFD predictive model would expand the interpretation of the flammability map results. Also such a result would allow a prediction of burning for materials outside the mapping by allowing a computation to indicate external heating they would need.

Table 4. Science data end products.

Objective	Science Data End Products
1. Observe burning behavior in long-duration microgravity for CH_4/N_2 and $\text{C}_2\text{H}_4/\text{N}_2$ mixtures on porous circular burners of 25 and 50 mm diameter. Consider O_2/N_2 ambients with various pressures and ambient O_2 concentrations and pressures. Emphasize conditions that can be related to diverse condensed fuels.	Color flame images and shapes. UV images. Surface temperatures and incident flame heat flux measurements. Radiation from the flame to the surroundings to estimate radiative flux. Flammability mapping of quasi-steady burning as a function of heat of combustion, heat of gasification, and surface temperature. Quasi-steady burning flux (burning rate per unit area) as a function of significant properties, e.g., heat of gasification, heat of combustion, and smoke point. Contour plots of soot temperature and filament temperature. Contour plots of soot volume fraction. Plots of radiant emissions versus time. Plots of chemiluminescent emissions versus time.
2. Consider the conditions of Objective 1 for ambients of O_2/CO_2 (desired).	Same as for Objective 1.
3. Consider the conditions of Objectives 1 – 2 for extinction limits.	Extinction limit map.

2.5 Justification for Extended-Duration Microgravity

Fire in a spacecraft microgravity environment is a likely event based on limited accident data, tests to burn materials, and research that has explored simple burning scenarios. Indeed, NASA screens the use of materials on spacecraft by its flammability Test 1.

Currently NASA Test 1 and Test 2 are incapable of directly analyzing material fire hazards in spacecraft. There is no predictive methodology to extrapolate from these tests. However, NASA Test 2, the Cone Calorimeter, is capable of determining heats of combustion and gasification, and surface reradiation in burning. Steady (or quasi-steady) burning rate data from the BRE in flight experiments will establish a flammability mapping in terms of these properties for microgravity. In addition, using Eq. (2), the results can establish the necessary heat flux condition for other fuels to burn in microgravity. The BRE is an efficient way to achieve quasi-steady burning. While microgravity tests of condensed fuels have been performed and are planned, they are limited in their ability to reveal sufficient information about the diverse condensed fuels that exist aboard the ISS. Moreover the time to achieve quasi-steady burning rate of solid fuels can be of the order of minutes as dictated by the time response of the solid. The BRE can be turned on and off quickly, and its quasi-steady condition is only dependent on

the gas phase phenomenon. While this time is shorter, it can still be on the order of 10 seconds or more.

The proposed tests cannot be performed in parabolic aircraft owing to considerable g-jitter disturbances. While limited testing is possible in drop facilities, the characteristic times for the gas phase (approximately 20 s) and the burner surface temperature (approximately 40 s) preclude consideration of quasi-steady conditions. Preliminary testing in the NASA 5.2 s drop facility indicated the approach to quasi-steady burning, but longer tests are needed to confirm this tendency. The longer duration testing in the ISS with the efficient operation of the BRE can produce results only limited by the gas-phase response time.

3. EXPERIMENT REQUIREMENTS

This section does not include any requirements, but instead describes their importance in achieving the experiment objectives. The requirements have been incorporated into the ACME-SRD-001 Integrated Science Requirements Document (ISRD) (Stocker, 2010).

3.1 Requirements Discussion

Most of the BRE experiment requirements fall within the requirements established by the other ACME experiments, as detailed in the ACME ISRD. This section emphasizes requirements that are unique to BRE.

BRE Burners [ISRD 1.13]

The design of the BRE burners is critical to meeting the BRE objectives. The burners shall involve round porous plates through which gaseous fuel is fed and evenly distributed. These porous plates shall have diameters of 25 and 50 mm. Each burner shall contain two-heat flux meters flush with the porous plate surface and facing outward. The burners shall be positioned such that the burner axis is coincident with the CIR chamber axis within ± 2 mm (i.e., along its length) and orthogonal to the CIR chamber window axes. The plane of the CIR chamber window centers shall be 10 ± 2 mm downstream of (i.e., above) the burner outlet.

The burners used by the PI team for their ground-based research are shown in Figs. 14 and 15. It is suggested that the flight burners be made using a similar design. Glass beads of 4.8 mm diameter (50 mm burner) and 3.2 mm (25 mm burner) provide a porous matrix for the fuel flow in the burners. The beads are held between two perforated brass screens: one at the top of burner as the operating face and the other one 25 mm below it.

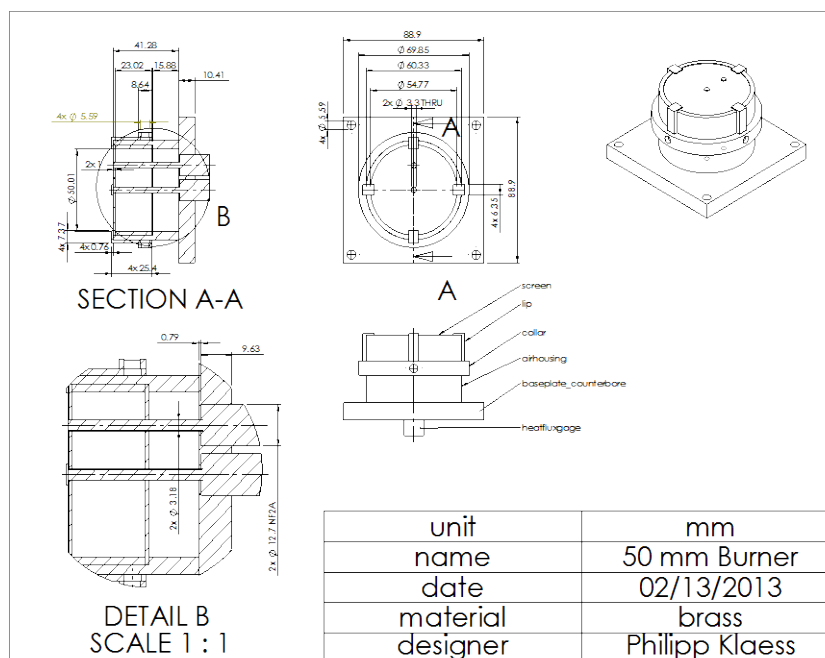


Figure 14. Burner with 50 mm porous surface.

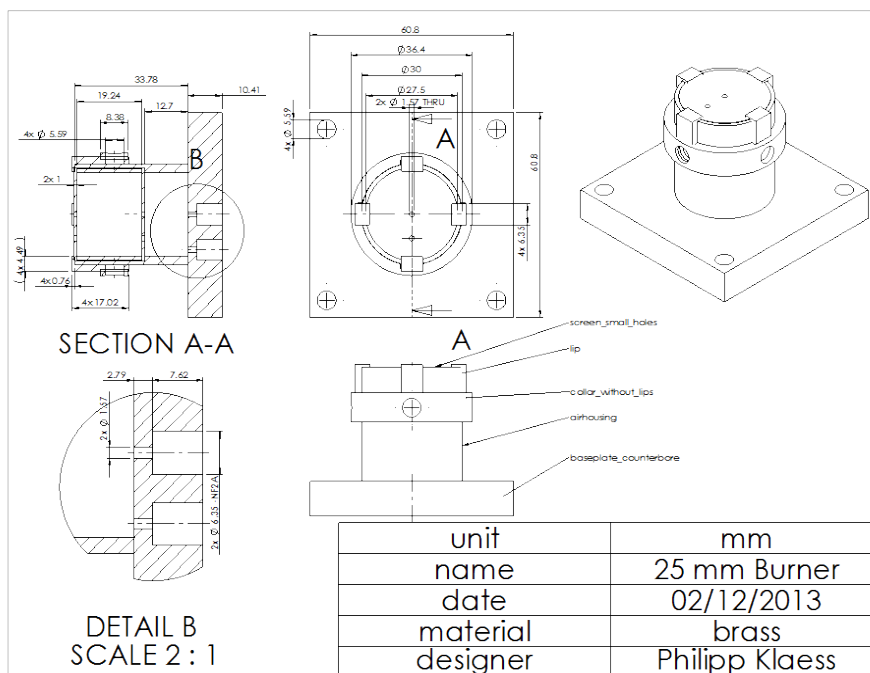


Figure 15. Burner with 25 mm porous surface.

Heat Flux Gages [ISRD 3.10]

Each burner should include two heat flux gages. For the 50 mm diameter burner these are at the center and 15 mm from the center, with a maximum diameter of 3.1 mm. For the 25 mm diameter burner, they are at the center and 10 mm from the center, with a maximum diameter of 1.5 mm. Each heat flux gage shall have a thermocouple at the sensor surface to identify conditions that could damage the sensor (200 °C). The sensor temperature will also affect the calibration of the device, the amount of re-radiation loss that occurs, and indicate possible water condensation.

The PI team is presently evaluating two models from Medtherm (models 8-1.8-10SB-4-0-36-20425AT and 4-10SB-1.4-0.43-4-36-21919T). O-rings are suggested to seal the heat flux gages at the base of each burner.

The recommended Medtherm sensors are from their 64 Series: Heat Flux Transducers and Infrared Radiometers for the Direct Measurement of Heat Transfer Rates. We used the Schmidt-Boelter gage that uses a multi-junction thermopile. This is important, as we want the surface of the sensor to be of a uniform temperature (unlike the alternative Gardon gage). A thermocouple also measures the temperature of the sensor. There is no transmitting window or aperture. The Medtherm thermopile gage has an absorptance of 0.95 over a spectral range of 0.6 to 15.0 μm . Currently we are using 10 mV output at a full range of 100 kW/m^2 . Recent drop tests indicate an initial heat flux of about 50 kW/m^2 at ignition and then dropping to values of generally about 5 kW/m^2 . As the Medtherm sensors can easily over range by 150%, within their linear calibration, we can exceed the 10 mV limit. The sensors have reported maximum non-linearity of $\pm 2\%$ of full range and a repeatability of $\pm \frac{1}{2}\%$. They are calibrated with an uncertainty of $\pm 3\%$. The maximum operating temperature is 400 °F (204°C). The sensor has a response time of less than 250 ms. For ground-based operation water-cooling is desired.

However, the sensor thermocouple specification is sufficient for operation without water, provided the sensor does not exceed about 200 °C.

Although 65-75 °C circulating water prevents possible water condensation and sensor overheating, there is no requirement for circulating water for the proposed flight hardware. Tests by the PI team have found that water condensation and sensor overheating are unlikely for the proposed flight test matrix.

Summary of the ISRD Sections that were Changed Significantly with the Addition of BRE

Burner Gas Delivery [ISRD 1.9]

The specific flow rates for BRE given as:

Fuel 0 to 1 slpm (on a nitrogen basis)

Inert 0 to 1 slpm (on a nitrogen basis)

These requirements were established by observations of flames in normal gravity and in the NASA Glenn 5 s drop facility, and by comparing these flames with those burning liquid fuels aboard the parabolic aircraft.

Ignition [ISRD 1.10]

It is suggested that ignition should occur at a distance of 3 mm from the rim of the porous burner surface. A centered igniter presumably will not lead to ignition because of a lack of sufficient oxygen.

Ambient Environment [ISRD 1.11]

Prior to each test, the chamber shall contain the specified gas composition, consisting of O₂ and inert (N₂ and CO₂, desired) within ± 0.01 mole fraction of each concentration. A cylindrical free area that is (1) at least 200 mm and as large as possible in diameter, (2) extends at least 100 mm and as far as possible downstream from the burner outlet, and (3) extends at least 50 mm and as far as possible upstream of the burner outlet shall be kept clear of solid objects. A second cylindrical free area (with the same axis as the first) that is (1) at least 150 mm and as large as possible in diameter and (2) extends at least 200 mm and as far as possible downstream from the burner outlet shall be kept clear of solid objects. The temporary insertion of the igniter and the presence of any probes (including TFP fibers and the gas-phase thermocouple) are allowed exceptions. Suggested methods to decrease bottled gas consumption rates include, as available, partial venting and filling, and scrubbing for CO₂ and H₂O.

Data Recording [ISRD 1.12]

Accepted with addition of data recording of the 2 BRE burner heat fluxes, the 2 heat flux sensor surface temperatures, and one more (i.e., total of 2) BRE burner temperature.

Monitoring Measurements [ISRD 2]

The BRE monitoring measurements shall include: chamber pressure; gas flow rates; burner pressure differential; and acceleration. These shall be initiated before test operations begin and continue sufficiently past flame extinction to allow a baseline measurement. In addition, the oxygen concentration should be measured before and/or after each test.

Science Diagnostics Requirements [ISRD 3]

The BRE science diagnostics measurements shall include: color imaging for operations; color imaging for data analysis (with a field of view of at least 90 mm in diameter); ultraviolet imaging (with a field of view of at least 75 mm in diameter); burner temperatures; gas phase temperatures; soot volume fraction (with a field of view of at least 45 mm in diameter); radiant emission; chemiluminescent emission; and post-test gas composition.

Color imaging [ISRD 3.1-3.2]

Color imaging will be used to determine flame size, shape, color, and existence. In addition, it will provide confirmation of other diagnostics used for detecting extinction limits. Visibly luminous soot will be observed with color cameras. Because flames can be asymmetric, a second view would minimize ambiguity. The field of view will need to be sufficiently large to observe the entire flame while at the same time be sufficiently small to allow for resolution of the fine scale needed to identify the onset of soot inception. For this reason, zooming capability is desired.

Burner Temperature [ISRD 3.4.1]

Accurate measurement of the burner surface is essential. For the burner surface, temperatures at 2 locations with a range of 30 – 500 °C are required to obtain the temperature of the exiting gas and the reradiation of the burner surface. These thermocouples should be located on a radius, opposite to the heat flux gages. One should be 5 mm from the burner center, and the other at a radius of 15 mm (for the 50 mm burner) and at a radius of 10 mm (for the 25 mm burner). The thermocouples should be appropriately bonded, or held in good thermal contact, with the metal surface. The thermocouples should be Type K and have a diameter of 0.010” or less.

We have used bare thermocouple wire threaded to a point of contact on the burner, and that has worked satisfactorily. However, that implementation is tedious and subject to misalignment. A bonded and insulated thermocouple should be used.

In addition to the two burner surface thermocouples, each heat flux sensor should have a thermocouple, installed by the sensor manufacturer, on the sensor element. Each of the two sensor thermocouples are required, so there are four burner thermocouples total.

Gas Temperature [ISRD 3.4.2-3.4.3]

Accurate measurement of the gas temperature is essential. In the gas phase, temperatures of hot soot-containing regions in a 85 mm diameter region are required. Soot pyrometry [ISRD 3.4.2] and thin-filament pyrometry [ISRD 3.4.3] are desired for comparisons with numerical predictions.

Flame Radiation

Measurements of radiative losses from the flame are critical to establishing quasi-steady conditions and to estimating the surface incident radiative flux. Because the metal burner’s radiative emissions may be comparable to those of the flame, it is required that the radiative loss sensor should not view hot portions of the burner. This measurement is important to distinguish any radiation differences among the flame, and to provide a means to estimate the radiative component of the heat flux to the burner sensors.

This sensor should view the flame above the burner, and not view any hot burner surfaces. An aperture should define this viewing region. The sensor should not respond to heated gases by

conduction, nor to changes in pressure. A wide spectrally transmitting window, or sufficient distance from the burner, should avoid conduction effects.

Chemiluminescent Emission [ISRD 3.7]

Flame extinction will be inferred by photomultiplier tubes [ISRD 3.7] and imaging [ISRD 3.1-3.3]. To ensure that extinction has occurred, flow rate will be changed to a condition for which a quasi-stable flame had previously been observed. If the flame does not reappear, it can be assumed that the flame had extinguished. UV emission [ISRD 3.3] will also be used to indicate the presence of a flame. While it is generally believed that the existence of a hydrocarbon flame can be detected by observation of blue emission, this may not be the case with microgravity flames because these flames are extremely weak and we are attempting to produce some of the lowest temperature diffusion flames that have been produced.

3.2 Operational Sequence [ISRD 4.5]

The BRE operational sequence is shown in Table 5. Approximate times shown are at the start of each step. A single operational test procedure can accomplish two objectives, (1) and (2) as listed in 2.2. Both quasi-steady burning and extinction are accomplished by the sequence in Table 5, specifically item 6. The ignition process should commence for a given fuel mixture at about 1 g/m²s of hydrocarbon fuel. It will be increased accordingly until ignition occurs.

Table 5. BRE Operational Sequence

Action	Approx. Time
1. Ensure that the appropriate burner is installed. Preflow the burner fluent gas at the composition of the upcoming test point to flush the plumbing system.	
2. Establish chamber conditions. These consist of a set point pressure and species compositions, as specified in the test matrix. Conditions are obtained in four ways: from cabin air (desired); from the preceding test; from scrubbing and replenishing; or from a complete evacuation and recharge.	
3. Allow chamber contents to reach equilibrium. A hold time of 5 minutes is required for quiescent, isothermal, and well-mixed conditions.	
4. Take reference images (if applicable). Establish framing rates for video cameras. Begin color imaging. Begin monitoring measurements and wait 15 s.	
5. Commence fluent flow at a value to be uplinked. The initial value should correspond to about 1 g/m ² -s of hydrocarbon fuel. Energize igniter to ignite the flame and then retract the igniter. If ignition does not occur within 5 seconds, shut off the flow. A new value of flow rate will be specified by uplink. If the flame ignites, proceed to Step 6. Otherwise proceed to Step 7.	0 s 5 s
6. Set the flow rate to the test flow rate. Anytime during this step, if the flame extinguishes, or either heat flux sensor exceeds a critical temperature, stop the fuel flow. Continue until the surface burner temperatures become quasi-steady. Then reduce the flow rate in 10% increments of the test flow rate, hold for 15 s, and continue such reductions until extinction.	60 s
7. Stop fluent flow. Record reference images (if applicable). After 60 s terminate color imaging and monitoring measurements. Select data for downlink and downlink data.	

3.3 Test Matrix [ISRD 5.5]

The detailed test matrix is given in Table 6. Assuming a mean burn duration of 30 s, the total burn duration of the required matrix is 37 minutes. The tests will emphasize measurements of two types of flames: quasi-steady burning and extinction. Tests will involve various fuel compositions and flow rates. This is necessary to map the range of conditions expected for condensed fuel burning. These tests support Objectives 1 – 3.

Part of the rationale for the test matrix is to consider conditions associated with NASA's planned manned flight activities: 21% O₂ in N₂ at 1.01 bar; 26.5% O₂ in N₂ at 0.703 bar; and 34% O₂ in N₂ at 0.565 bar.

Table 6. BRE Test Matrix

Test	Ambient	Fluent	Pressure, bar	Fuel flow rate, sccm N ₂	Notes
1	21% O ₂ in N ₂	C ₂ H ₄	1.01	200	Test of system operation, diagnostics, and burning and extinction test. Use cabin air if possible. Use 25 mm burner.
		↓	↓		Evacuate and recharge chamber.
2	40% O ₂ in N ₂	↓	↓	200	Burning and extinction test.
3	↓	↓	↓	400	↓
4	↓	C ₂ H ₄	↓	100	↓
5	↓	75% C ₂ H ₄ in N ₂	↓	200	↓
6	↓	↓	↓	400	↓
7	40% O ₂ in N ₂	75% C ₂ H ₄ in N ₂	1.01	100	Burning and extinction test.
8–13	34% O ₂ in N ₂	C ₂ H ₄ in N ₂	0.565		Repeat Tests 2–7 for different ambient.
14–19	26.5% O ₂ in N ₂	↓	0.703		Repeat Tests 2–7 for different ambient.
20–25	21% O ₂ in N ₂	C ₂ H ₄ in N ₂	1.01		Repeat Tests 2–7 for different ambient.
26–49		CH ₄ in N ₂			Repeat Tests 2–25 for CH ₄ at the same mole fractions as C ₂ H ₄ .
50–73		C ₂ H ₄ in N ₂			Repeat Tests 2–25 for 50 mm burner.
74–97		CH ₄ in N ₂			Repeat Tests 2–25 for CH ₄ at the same mole fractions as C ₂ H ₄ and for 50 mm burner (desired).
98–103			2.02		Repeat Tests 20–25 at 2.02 bar (desired).
104–115	O ₂ in CO ₂		1.01		Repeat Tests 2–7 and 20–25 for CO ₂ ambient at the same mole fractions as N ₂ (desired).

Notes

¹Different fuel and oxidizer mole fractions may be specified during uplink.

²It may be necessary to ignite at different flow rates and/or gas compositions than those specified above.

³Assuming scrubbing capability is available, the CO₂ and H₂O will be scrubbed after some tests, and reactants replenished as needed.

⁴All tests use the 25 mm burner except tests 50 – 97.

3.4 Science Success Criteria [ISRD 6.5]

The BRE Science Success Criteria are shown below.

Minimum Success

- Obtain color video, burner surface temperature, and burner heat flux for two C₂H₄ flames that burn for at least 20 s and then extinguish.

High Success

All of the above plus:

- Obtain a flammability map for C₂H₄.

Complete Success (i.e., completion of required test matrix)

Table 6. BRE flight test matrix.

All of the above plus:

- Obtain a flammability map for CH₄.
- Measure peak temperatures (using filament and/or soot pyrometry) as a function of time for at least 5 flames.
- Measure temperature distributions (using filament and/or soot pyrometry) at or near quasi-steady conditions for at least 5 flames.
- Measure temperature distributions (using filament pyrometry) near the extinction limit for at least 5 flames.
- Measure soot volume fraction profiles at (or near) quasi-steady conditions and near the extinction limit for at least 5 flames.

Superior Success (desired)

All of the above plus:

- Complete the desired parts of the test matrix.

3.5 Post Flight Data Analysis Plan

The proposed test matrix is intended to shed light on the burning of condensed fuels in microgravity. We plan to examine conditions that map out flammable conditions and burning rates of diverse condensed fuels. This will result in extensive image data.

Much of the post-flight data analysis will occur during mission operations as the science team evaluates each set of test runs in preparation for subsequent runs. Analysis of these tests will include: tracking of flame size and shape; analysis of discrete signals (e.g., thermocouples, radiometers, photomultipliers, and pressure transducers) for evidence of the quasi-steadiness of the flames; analysis of the temperature profiles (thin filament and soot temperature) to compare with model predictions; and de-convolution of soot volume fraction measurements. The PI team understands that NASA will furnish only raw data, and that the PI team will be responsible for converting this to measurements of soot temperature, soot volume fraction, etc.

The flammability maps will be prepared on 3-axis plots where the axes are burner heat of combustion, heat of gasification, re-radiation heat flux (See Figure 13). Alternatively these will be presented as contour plots. Flame temperatures near extinction will be determined either by de-convolution of the soot temperature data or by thin fiber pyrometry.

4. REFERENCES

- Ali, S., Raghavan, V. and Rangwala, A. 2010. A Numerical Study of Quasi-Steady Burning Characteristics of a Condensed Fuel - Effect of Angular Orientation. *Combustion Theory and Modeling*, **14**, 495-518.
- Brahmi, L., Vietoris, T., Rouvreau, S., Joulain P., David L. and Torero, J.L. 2005. Microgravity Laminar Diffusion Flame In A Perpendicular Fuel And Oxidizer Streams Configuration. *AIAA Journal*, **43**, 1725-1733.
- Bustamante, M.J., Dotson, K.T., Zhang, Y., Sunderland, P.B. and Quintiere, J.Q. 2012. Laminar Burning on Flat Wicks at Various Orientations. *Spring Technical Meeting of the Central States Section of the Combustion Institute*.
- de Ris, J. and Orloff, L. 1975. The role of buoyancy direction and radiation in turbulent diffusion flames on surfaces. *Symposium (Intl.) on Combustion*, **15**, 175-182.
- Dietrich, D.L., Ross, H.D., Shu, Y., Chang, P. and T'ien, J.S. 2000. Candle Flames In Non-Buoyant Atmospheres. *Combustion Science and Technology*, **156**, 1-24.
- Downey, B. P. 2009. An investigation of the UL-94V plastics flammability test. *M.S. Thesis*, University of Maryland, College Park.
- Kim, J.S, de Ris, J. and Kroesser, William F. 1971. Laminar free-convective burning of fuel surfaces. *Symposium (Intl.) on Combustion*, **13**, 949-961.
- Kimzey, J. H. 1974. Skylab Results: Proceedings of the 3rd Space Processing Symposium Vol.1. *NASA TM-X-70752: Marshall Space Flight Center*, 115-130.
- Li, L. and Sunderland, P.B. *An Improved Method of Smoke Point Normalization*, Combustion Science and Technology 184 (2012) 829-841.
- NASA Marshall Space Flight Center. 1998. NASA STD-6001.
- Ohlemiller, T. J. 1992. An Assessment of the NASA Flammability Screening Test and Related Aspects of Material Flammability. NISTIR 4882, NASA CR-189226.
- Orloff, L. and deRis, J. Modeling of Ceiling Fires. *Symposium (Intl.) on Combustion*, **13**, 979-992.
- Quintiere, J. Q. 2006. *Fundamentals of Fire Phenomena*. John Wiley & Sons Ltd., Chichester, UK.
- Quintiere, J.Q. and Rangwala, A.S. 2004. A theory for Extinction based on Flame Temperature. *Fire and Materials*, **28**, 387-402.
- Ross, H.D. 2001. *Microgravity Combustion*. Academic Press, San Diego.
- Stocker, D.P. ACME (Advanced Combustion via Microgravity Experiments) Integrated Science Requirements, Revision A, NASA Glenn Research Center, April 24, 2010.
- Sunderland, P.B., Mendelson, B.J., Yuan, Z.-G. and Urban, D.L. 1999. Shapes of Buoyant and Nonbuoyant Laminar Jet Diffusion Flames. *Combustion and Flame*, **116**, 376-386.
- Takahashi, F., Hennigan N., Stocker ,D. P., Ferkul, P. V., Katta, V. R., "Characteristics of Laminar Diffusion Flames in a Quiescent Microgravity Environment", 8th U. S. National Combustion Meeting, University of Utah, May 19-22, 2013.
- Tewarson, A. 2002. Generation of Heat and Chemical Compounds in Fires. *SFPE Handbook*, 3-82.

APPENDIX 1: Appended papers.

1. Y. Zhang, M.J. Bustamante, M.J. Gollner, P.B. Sunderland, J.G. Quintiere, Burning on Flat Wicks at Various Orientations, *Journal of Fire Sciences* (accepted).
2. Y. Zhang, M.J. Bustamante, P.B. Sunderland, J.G. Quintiere, P. Ferkul, *A Burning Rate Emulator for Study in Microgravity*, 8th U.S. National Combustion Meeting, Salt Lake City (2013) 14 pp.

Burning on Flat Wicks at Various Orientations

Zhang, Y., Bustamante, M.J., Gollner, M.J., Sunderland, P.B., Quintiere, J.G.*

Dept. of Fire Protection Engineering, University of Maryland, College Park, MD 20742, USA

*Corresponding author email: jimg@umd.edu

ABSTRACT

Burning on flat plates was studied at various orientations with respect to gravity. Flat wicks of ceramic (Kaowool PM) board (10 cm wide and 1 – 10 cm long) were saturated with methanol or ethanol. Steady flames were obtained that ranged from boundary layer flames to plume-type burning. The onset of unsteady flow and transition to turbulence commenced at Grashof numbers of $10^6 - 10^7$, increasing with decreasing angle (towards underside burning). The average burning rate per unit area was recorded along with the flame location. Experiments on PMMA were used for comparison with the liquid-wick results. The results roughly correlated with laminar pure convective theory, and improved results were indicated when the gravity term associated with the pressure gradient normal to the plate was included. Theoretical results by the integral-method to reduce the PDE's to ODE's are presented.

KEYWORDS: Buoyancy, burning rate, combustion, flame standoff, inclined plate.

NOMENCLATURE

B	Spalding B number $\frac{Y_{o,\infty}\Delta h_c/s - \tau_0}{L}$	Y	mass fraction
c	Eq. (1c)	Greek	
c_p	specific heat of gas	ζ_f	dimensionless flame location, Eq. (1c)
\bar{c}_p	mean specific heat	θ	angle between x and Y
Gr_l	Grashof number	μ	dynamic viscosity
Gr_l^*	modified Grashof number, $\frac{g \cos \theta L}{4\bar{c}_p T_\infty} \frac{l^3}{\nu \infty^2}$	ν	kinematic viscosity
Δh_c	heat of combustion	Σ	Eq. (2c)
k	thermal conductivity	ρ	density
l	plate length	τ_0	$\frac{\bar{c}_p(T_w - T_\infty)}{L}$
L	heat of gasification	Ω	Eq. (1b)
\dot{m}''	mass flow per unit area	Subscripts	
Pr	Prandtl number, $\mu c_p/k$	0	initial
Ra_l^*	modified Rayleigh number, Eq. (2b)	f	flame
s	oxygen to fuel stoichiometric ratio	F	fuel
S	$Y_{o,\infty}/sY_{F,T}$	T	condensed phase
T	temperature	o	oxygen
x	coordinate along plate	w	wall
y	coordinate normal to plate	∞	ambient
y_f	flame standoff distance	v	vaporization
Y	direction with gravity vector		

INTRODUCTION

This study examines steady burning on flat plates of lengths from 1 – 10 cm long with orientations ranging from vertical ($\theta = 0^\circ$) to horizontal, burning on the top (+) or bottom (-). While work has been performed for the purely vertical and horizontal cases, little has been done for other orientations. Early work by Blackshear and Murty [1] examined the effect of orientation for a square plate 15.9 cm ranging from horizontal bottom ($\theta = -90^\circ$) to top burning ($\theta = +90^\circ$). For that arrangement they found that the average burning rate achieved a maximum at -50° , dropping off slightly to -90° , and much more steadily to $+90^\circ$. They and others [1-7] more thoroughly examined the purely horizontal or vertical orientations. Blackshear and Murty [1, 2] explained their results through the B number and the heat transfer coefficient. Kosdon and Williams [3] were the first to develop a laminar boundary layer theory for the burning of a vertical fuel surface. They noted that their prediction of the flame standoff position was about

1.5 times higher than their data. de Ris et al. [4, 5] extended their analysis to both vertical and horizontal underside burning, obtaining analytic solutions by the Pohlhausen integral method. Ahmad and Faeth [6, 7] examined both the laminar and turbulent cases following a similar theoretical approach. Investigators have conducted experiments that included the use of solid materials, ceramic plates saturated with liquid fuels, and burners to simulate real materials. Measurements on PMMA have been carried out by Ohtani et al [9] and Gollner et al [10]. More recently a direct numerical solution (DNS) of the full equations by Ali et al. [8] was obtained for a 1 cm plate at various orientations. The onset of instability from laminar flow over hot inclined plates has been reported by Lloyd and Sparrow [11] and Al-Arabi et al [12]. The current work was motivated by considering the use of burners to emulate the burning of real materials, in a non-Earth-gravity environment.

This study follows the approach by Ahmad and Faeth [6, 7], extending their work to steady burning at multiple orientations. We use their experimental technique of porous ceramic plates soaked with liquid fuels of methanol and ethanol. We also adopt their theoretical integral modeling approach. In our model, however, we add an additional term describing the role of cross flow buoyancy normal to the plate. This term is the sole buoyancy term in the ceiling burning orientation of Orloff and de Ris [5]. Except for the DNS solution of Ali et al. [8], all previous boundary layer analyses ignored this effect and only considered the buoyancy component in the flow direction parallel to the plate. This parallel component does not differentiate between top and bottom burning for the same plate angle.

EXPERIMENTAL

The experiments used ceramic wicks, as shown in Fig. 1. They were soaked with methanol or ethanol. The pyrolysis region and surrounding border were constructed of 3.2 mm thick Kaowool PM and were backed with 12.7 mm thick Kaowool 3000 to minimize heat loss to the sides and rear of the fuel laden area. Sodium silicate was applied to the interface of the plate with the border to eliminate leakage of the liquid fuel.

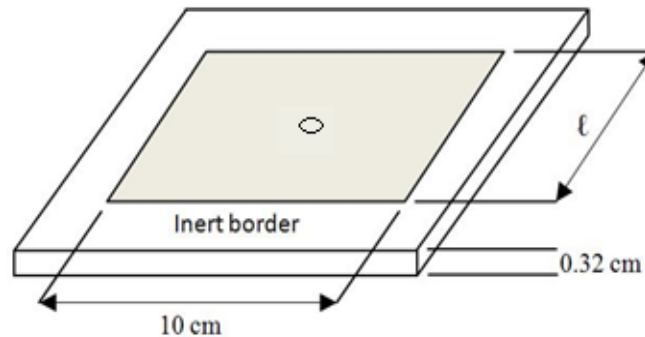


Figure 1. Sketch of a typical wick with a heat flux gauge located in the center.

10 cm wide flat wicks of length 1, 2, 3, 4, 6, 8, and 10 cm were constructed. Wicks were affixed to a stand capable of rotating 180° with respect to gravity. The mass of the wick was measured over time with a load cell, the mass-loss rate or burning rate determined by the slope of the linear mass versus time curve. The flame standoff distance was recorded during steady burning using photographs recorded parallel to the plate. The photographs were analyzed to obtain instantaneous plots over the length of the plate. Additional details of these measurements can be found in Bustamante [13], along with heat flux results for 10×10 cm methanol soaked wicks with a 3 mm Schmidt-Boelter sensor heat flux transducer located at the center of the plate.

Flame Shape

Figure 2 shows an array of instantaneous methanol flame images for the various burning orientations and plate lengths (with a fixed width of 10 cm). The images show that an increase in pyrolysis length increases fluctuations downstream of the leading edge beginning a transition to turbulence. Top burning plates show that buoyancy can cause separation of the boundary layer from the plate, resembling a plume-like flow. Beyond the plate, a wake plume occurs. For the pool fire case, the flame behavior changes from unsteady laminar flow to turbulent flow with increasing distance from the base and increased pyrolysis length. For the bottom ceiling fire case, the flame is blue and always laminar. Figure 3 shows these images in terms of digitized flame standoff locations at several instants of time when “steady average plate burning” occurred. The flame clearly begins to become unsteady at some locations.

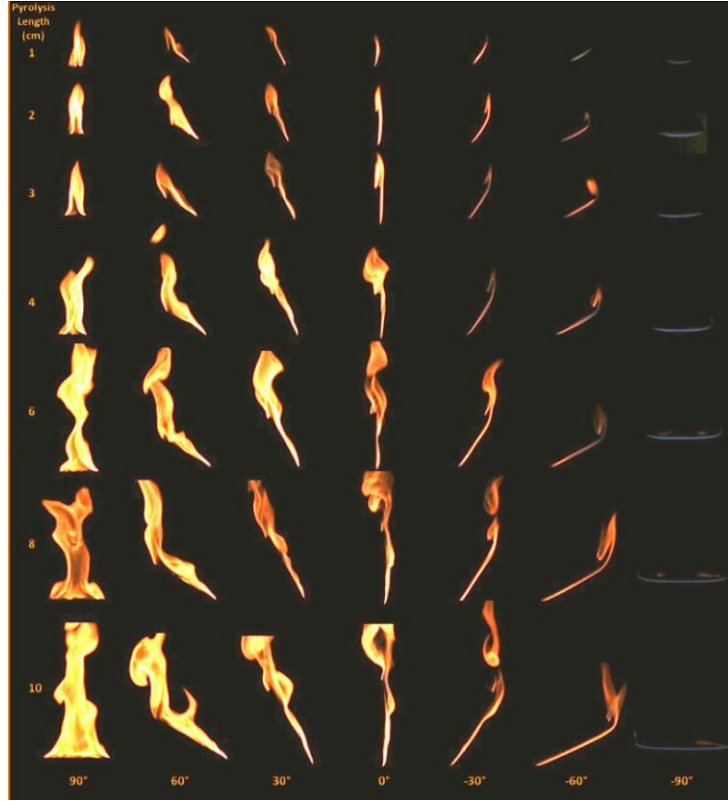


Figure 2. Methanol flame shapes at various orientations and plate (pyrolysis) lengths.

In theory, for the boundary layer flow orientations, the flame location should only be a function of the position (x) for all plate lengths. Figure 4 shows the methanol flame locations for a given angle for all of the plate lengths. In the laminar steady regions, this behavior shows the similarity of the flame location with distance. The departure from laminar flow to the onset of turbulence or plume flow is seen for the longer plates. Data for ethanol indicates that, for the laminar flows, the bottom flames are slightly thicker than the vertical or top flames.

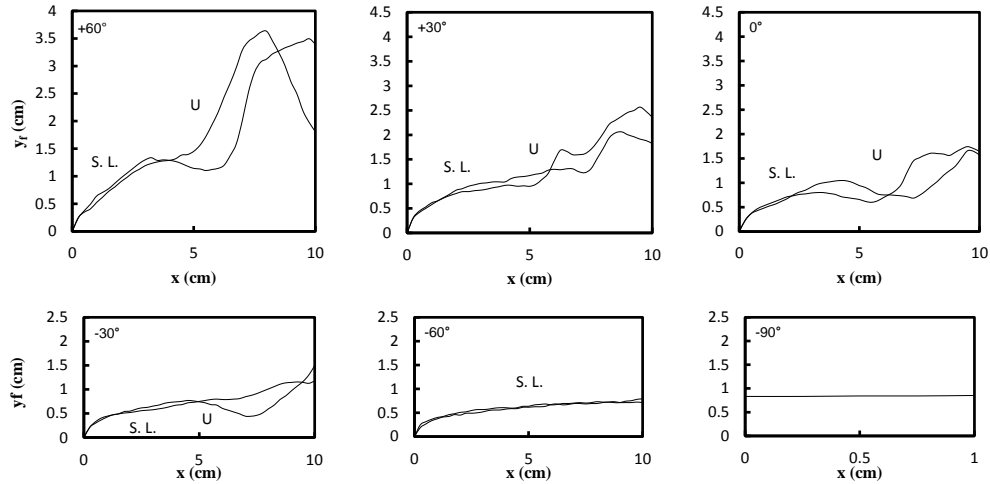


Figure 3. Measured methanol flame locations for the 10 cm long plate at all orientations. S.L. means steady laminar flow; U indicates the onset of unsteady flow. From upper left and going clockwise these are Figs. a, b, c, d, e, and f.

These data can be analyzed in terms of a Grashof number (Gr) in order to generalize the departure from steady laminar flow. The Gr at which the unsteady flow begins is seen to increase from about 10^6 to 10^7 as the orientation of burning changes from the top to the bottom of the plate, as shown in Figure 5. Predominately steady laminar flow is observed for plates at -60° and -90° for lengths up to 10 cm. For these angles, the Grashof number for transition shall be greater than 4×10^7 . Some heat-transfer studies also found a decreasing Gr under which transition occurs when inclining heated surfaces of a plate from top to bottom [11, 12]. Their Gr for the end of the laminar region, however, are somewhat higher and follow a more extreme slope in comparison to this study, perhaps because they were not reacting flows which may induce an earlier transition due to large temperature gradients in the boundary layer.

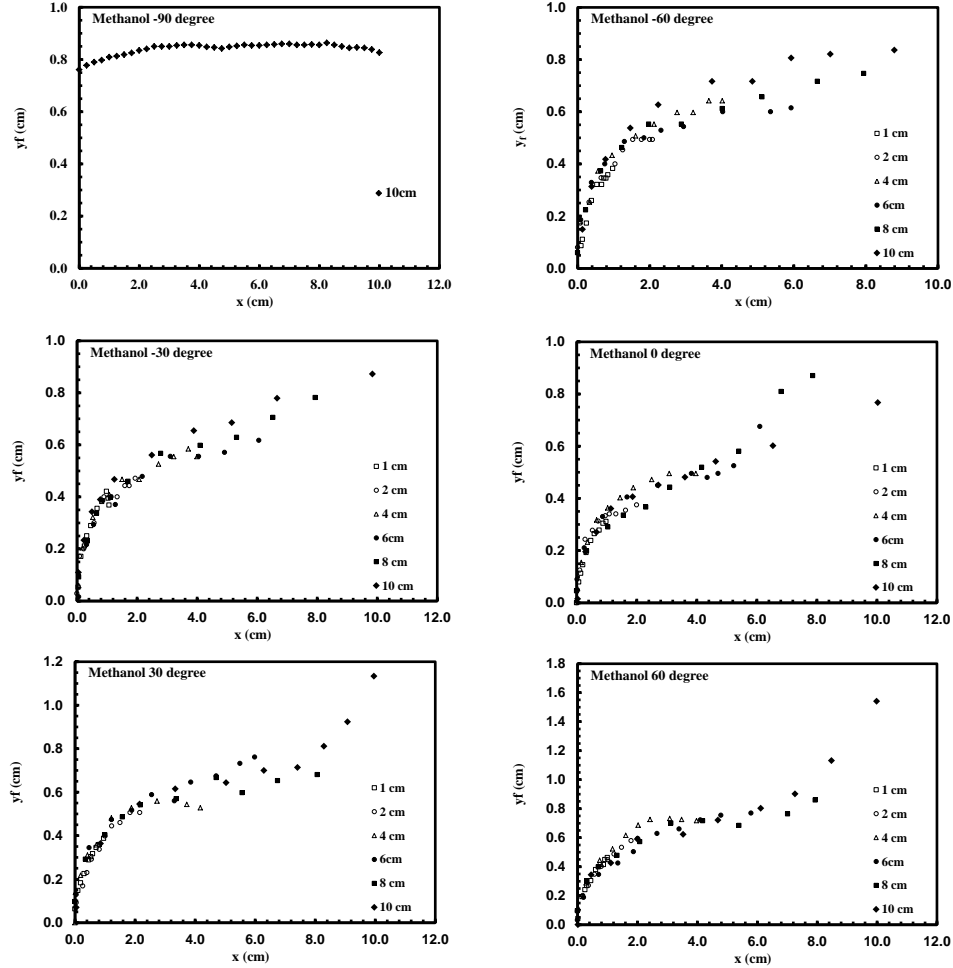


Figure 4. Methanol flame locations for all plate lengths as a function of angle.

Average Burning Rate

The average burning rate per unit area of the plate surface was determined for each plate length, orientation, and fuel. The steady values are reported, and contain some results where periodic unsteadiness occurs due to the onset of turbulence or plume-like flow. These data for all orientations and plate lengths of 1, 4, and 10 cm are shown in Fig. 6a for methanol and Fig. 6b for ethanol. As the length of the plate decreases the burning rate increases, consistent with increasingly laminar flow for shorter lengths. At very small lengths ($l = 1$ cm in Figure 6), the heat transfer to the plate is predominant, and therefore fuel vaporization rates significantly increase as the flame anchors close to the fuel surface over a large portion of the short length.

There is a distinct maximum at $+30^\circ$ (burning on the topside) for $l = 1$ cm, and this maximum diminishes with plate length. Blackshear and Murty [1], on the contrary, found a maximum at -50° (underside) for a plate of 15.9 cm.

Their plate length would primarily result in turbulent flows (lower burning rates), except for burning on the underside in which laminar burning would be highest, accounting for their differences.

There is little difference between the data for methanol and ethanol in this study. Figure 7 shows a more complete set of data for all lengths and orientations. The trend to larger lengths suggests why the maximum could shift from the topside to the bottom side in the data of Blackshear and Murty [1].

ANALYSIS

In order to explain the behavior of the data, the theoretical results of Ahmad and Faeth (A-F) [6, 7] are examined. As our flow is mostly laminar, with some unsteadiness, we use their laminar analytical solution. We also use their properties, as listed in Table 1. Their solution applies to boundary layer flows (-60° to $+60^\circ$ of our data), and accounts for the angle of inclination by the component of gravity along the plate using $\cos\theta$, but does not discriminate between top and bottom burning.

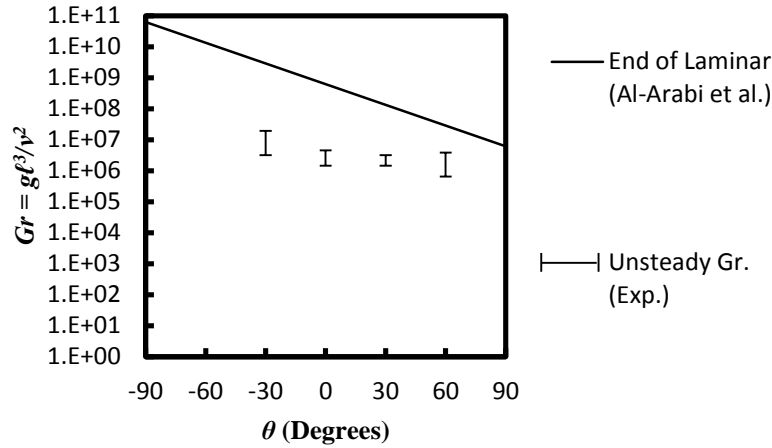


Figure 5. The Grashof number at the onset of unsteady laminar flow as a function of plate angle. The Grashof number by Al-Arabi et al. is plotted based on a flame temperature of 2200 K.

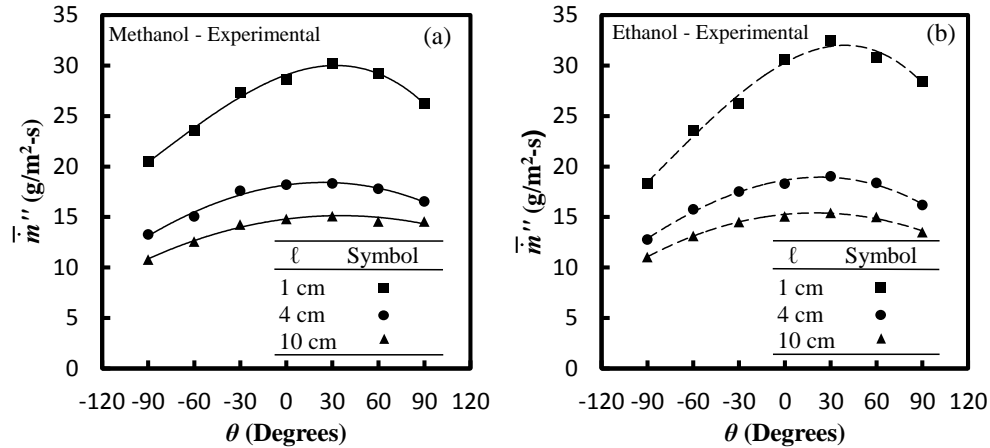


Figure 6. Burning rate per unit area as a function of orientation for plates 1, 4 and 10 cm.

Their results follow for the average flame standoff distance,

$$\left(\frac{y_f}{x}\right) Gr_x^{*1/4} \Omega = 3.6, \quad (1a)$$

where

$$\Omega = \left[\frac{BPr}{c^2 \ln(1+B)} \right]^{1/2} \left[\frac{3(B+\tau_0)\zeta_f + \tau_0}{(1+B)(2+2B+Pr)} \right]^{1/4}, \quad (1b)$$

$$c \equiv \left(\frac{L}{4\bar{c}_p T_\infty} \right) \left[4(B + \tau_0)\zeta_f + B \left[(1 - \zeta_f)^4 - 1 \right] \right] + \zeta_f \quad (1c)$$

and

$$\zeta_f = 1 - \left[\left(\frac{B+1}{B} \right) \left(\frac{S}{S+1} \right) \right]^{1/3} \quad (1d)$$

with $S \equiv \frac{Y_{O,\infty}}{SY_{F,T}}$ and $Y_{F,T} \equiv 1$.

In the later part of this paper, it will be shown that for most non-charring materials, Ω is approximately 0.3.

The average mass burning rate per unit area is also given by A-F,

$$\bar{m}'' \ell Pr^{3/4} \Sigma Ra_\ell^{*-1/4} / \mu_\infty = 0.934. \quad (2a)$$

Here the number on the right-hand-side (RHS) of Eq. 2a differs slightly from the A-F [6, 7] result of 0.66, which we believe due to a computational error. The modified Rayleigh number in Eq. 2a is

Table 1. Fuel properties from Refs [6, 7]

Property	Methanol	Ethanol	PMMA
Molecular Weight (g/mol)	32.04	46.07	100
Boiling Temperature (K)	337.7	351.5	668
L (kJ/kg) ^b	1226	880	1600
c_p (kJ/kg-K) ^b	1.37	1.43	1.19
μ_{air} (x 10 ⁻⁵) (N-s/m ²) ^b	1.8	1.8	1.8
B	2.6	3.41	1.6
s	0.154	0.111	0.21
τ_0	0.044	0.087	0.082
Pr	0.73	0.73	0.73
ζ_f^a	0.430	0.494	0.344
$\bar{\rho}/\rho_\infty$ @ 1000 °C	0.234	0.234	0.234
Σ	0.78	0.628	1.16
Ω	0.34	0.308	0.48

Ambient air taken to be at 298K:

$\nu_\infty = 15.3 \times 10^{-6} \text{ m}^2/\text{s}$.

^a Calculated parameter

^b Taken at boiling point of fuel

$$Ra_\ell^* = Pr Gr_\ell^* = Pr \left[\frac{Lg\ell^3 \cos(\theta)}{4\bar{c}_p T_\infty \nu_\infty^2} \right], \quad (2b)$$

where

$$\Sigma = \left[\frac{1+B}{B \ln(1+B)} \right]^{1/2} \left[\frac{1 + \frac{0.5Pr}{1+B}}{3(B+\tau_0)\zeta_f + \tau_0} \right]^{1/4}. \quad (2c)$$

Full variable definitions are given in the nomenclature. The coordinate system is shown in Figure 8. In both equations 1a and 2a, the RHS should depend on the angle if there are differences between top and bottom burning.

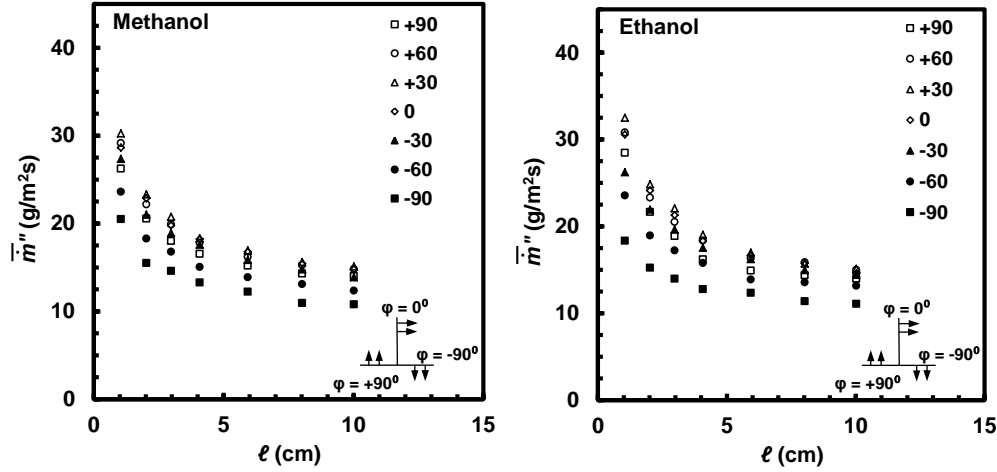


Figure 7. Average mass flux from integral model and experimental results of (a) methanol and (b) ethanol for wick lengths of 1, 2, 3, 4, 6, 8, and 10 cm at angles from -90° to $+90^\circ$.

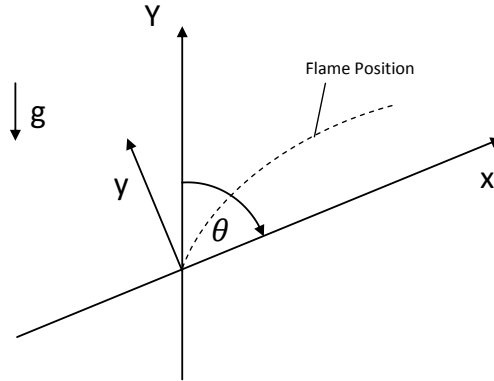


Figure 8. Coordinate system and gravity vector

The dimensionless flame standoff distance is shown in Fig. 9 according to Eq. (1). The results contain orientations of $+60^\circ$ (top burning) to -60° (bottom burning), for wick lengths including 1, 2, 3, 4, 6, 8, and 10 cm. The variation bars represent differences from different sample lengths ($l = 1 - 10$ cm). The dimensionless result should collapse the two fuels, but some difference is observed. This could be due to property effects or from neglecting radiation in the model. The correlation suggests an independence with angle within about 30%, but the theory is over twice as high. Kosdon and Williams [3] similarly found their theory over-predicted experimental flame standoff distances by about 1.5 times. Flame standoff measurements from experiments on PMMA [12] are not shown because they were based on observation of a yellow flame, not comparable to measurements in this study of the blue flame, closer to the plate surface.

The dimensionless burning rates from this study are plotted in Figure 10, along with data for 10×20 cm PMMA (20 cm pyrolysis length) by Gollner et al. [10] and 3-10 cm square sheets of PMMA by Ohtani et al. [9]. The Grashof number for the wick lengths of 1- 10 cm ranges from 10^4 to 10^7 . For the 20 cm length of PMMA burning, the Grashof number is about 3×10^8 , which falls within the range of transition from laminar to turbulence ($10^8 - 10^{10}$). Here the results indicate an increase in burning rate as the angle increases from -60° (bottom) to $+60^\circ$ (top burning). The two liquid fuels show this same trend, but do not collapse to within about 10%. The PMMA data, containing a mostly laminar flame over its length, also shows a similar trend with angle, but lower in magnitude. Again the theory over predicts the flame standoff distance and indicates an effect of the angle of inclination. A constant of about 0.6 would embrace most of the liquid wick data to within about 25% while ignoring the distinct trend with angle. The numerically-solved burning rate is plotted along with the experimental data. As the experimental ones,

they are solved for wick lengths of 1, 2, 3, 4, 6, 8, and 10 cm and the plotted result is the average over those multiple lengths. Adding additional cross-flow term helps to deviate the top burning from bottom burning. The numerical result almost follows the same trend as the averaged experimental data with respect to inclinations. By including the cross-flow effect, the theory yields a better prediction with respect to burning phenomena at different inclinations. These numerical results will be discussed in detail later and address the cross-flow buoyancy term neglected in the Ahmad and Faeth analytical solution.

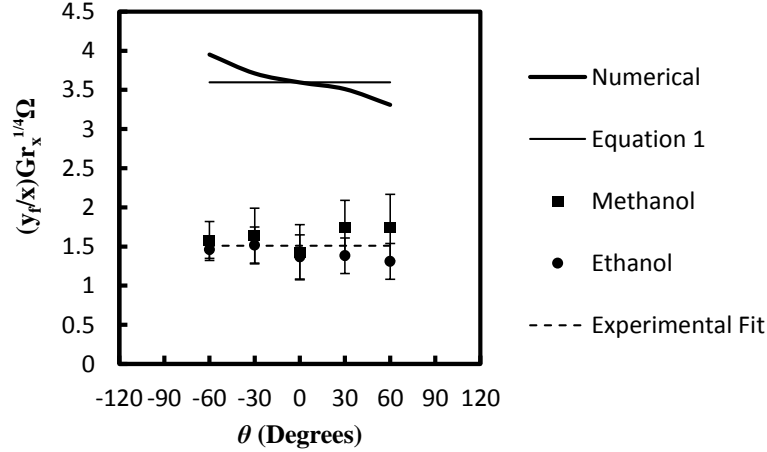


Figure 9. Dimensionless flame standoff for the full set of data. Symbols indicate average dimensionless standoff for all lengths with vertical bars indicating the variability with angle. Equation 1 $\left(\frac{y_f}{x}\right) Gr_x^{*1/4} \Omega = 3.6$ is derived from Ahmad and Faeth. Numerical calculation is based on modified equations from this study and a fit of experimental data is shown.

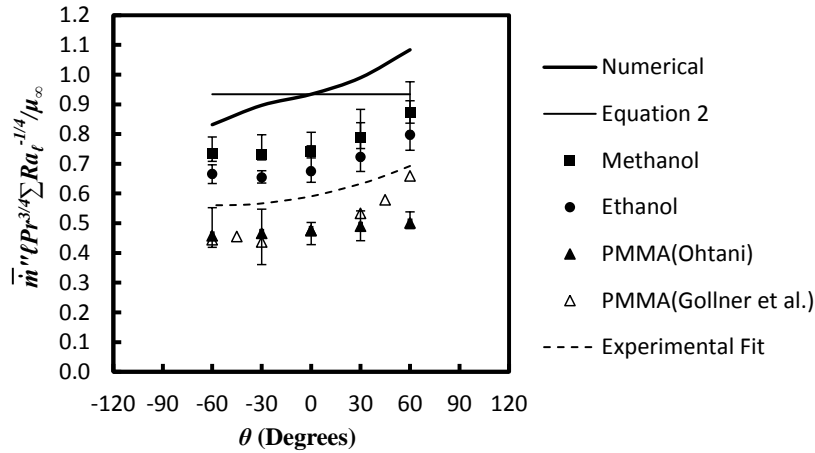


Figure 10. Dimensionless burning rate for the full set of data. Symbols indicate average burning rates with vertical bars indicating the variability. Equation 2, $\bar{m}'' \ell Pr^{3/4} \Sigma Ra_\ell^{*-1/4} / \mu_\infty = 0.934$ is derived from Ahmad and Faeth. Numerical calculation is based on modified equations from this study and a fit of experimental data is shown.

Based on the data presented in Figure 10, a trend line going through the average values of the data points can be formulated as a function of the inclination

$$\frac{\bar{m}'' \ell Pr^{3/4} \Sigma Ra_\ell^{*-1/4}}{\mu_\infty} = 0.0154(\tan \theta)^2 + 0.0399 \tan \theta + 0.5953. \quad (2d)$$

In the numerical study by Ali et al. [8], a fit by them of the effect of orientation gives a dependence very similar to our behavior in Fig. 10. The parameter Σ is plotted as a function of B in Fig. 11. Σ is calculated using parameters of

a range of materials given in Table 2. For non-charring materials ($B > 0.8$), a simpler expression for Σ is found solely depending on B ,

$$\Sigma = 1.6B^{-0.74}. \quad (2e)$$

Together, a functional relationship for the burning rate based on the B number and angle of inclination is

$$\frac{\bar{m}'' \ell Pr^{3/4} Ra_\ell^{*-1/4}}{\mu_\infty} = \frac{0.0154(\tan \theta)^2 + 0.0399 \tan \theta + 0.5953}{1.6B^{-0.74}}. \quad (2f)$$

The parameter Ω is plotted in a similar way. For non-charring materials, Ω remains nearly constant with a value of 0.3 for most of the materials. Thus, equation (1a) becomes

$$\left(\frac{y_f}{x}\right) Gr_x^{*1/4} = \frac{3.6}{0.3} = 12, \quad \text{for } B > 0.8. \quad (2g)$$

Table 2. Estimated dimensionless properties including Ω and Σ .

Material	Δh_c^a (kJ/g)	L^a (kJ/g)	T_v^a (°C)	B^a	Ω^b	Σ^b
<i>Liquids</i>						
n-Hexane	42	0.45	69	6.7	0.28	0.41
n-Heptane	41	0.48	98	6.2	0.28	0.43
n-Octane	41	0.52	125	5.7	0.27	0.44
Benzene	28	0.48	80	6.2	0.31	0.44
Toulene	28	0.50	110	5.9	0.31	0.45
Naphthalene	30	0.55	218	5.2	0.29	0.47
Methanol	19	1.2	64	2.5	0.36	0.8
Ethanol	26	0.97	78	3.1	0.31	0.67
n-Butanol	35	0.82	117	3.6	0.28	0.59
Acetone	28	0.58	56	5.2	0.4	0.6
<i>Solids</i>						
Polyethylene	38	3.6	360	0.75	0.27	2.02
Polypropylene	38	3.1	330	0.89	0.27	1.72
Nylon	27	3.8	500	0.68	0.32	2.25
Polymethylmethacrylate	24	2.0	300	1.4	0.31	1.2
Polystyrene	27	3.0	350	0.91	0.31	1.73
<i>Solids, charring</i>						
Polyurethane foam, rigid	17	5.0	300	0.56	0.52	3.08
Redwood	12	9.4	380	0.29	3.62	8.26
Red oak	12	9.4	300	0.30	3.14	8.07
Maple	13	4.7	350	0.58	0.68	3.08

- a. Quintiere, J. G., *Fundamentals of Fire Phenomena* [16]
- b. Eq. 1b
- c. Eq. 2c

MATHEMATICAL MODEL

Here the model of Ahmad and Faeth [6, 7] is considered, except now the pressure gradient of the normal momentum equation is included. This effect produces an additional buoyancy term that aligns with the main flow direction. It will be called “the cross-flow effect (CF)”. This effect of the fuel surface is included to help differentiate between burning at the top and the bottom for the same inclination. We wish to see if this inclusion explains the behavior of

the correlations of Eq. (1) and (2) with the data. The following assumptions are taken into account in the development of the model:

- The ambient atmosphere has a constant temperature and composition.
- Density does not change strongly with x .
- The flame is laminar, two dimensional and steady.
- Boundary layer assumptions apply.
- The flow is a mixture of an ideal gas with a constant specific heat and unity Lewis number.
- Radiation and viscous dissipation are neglected.
- The combustion process is a single global chemical reaction.
- The flame sheet assumption is taken.

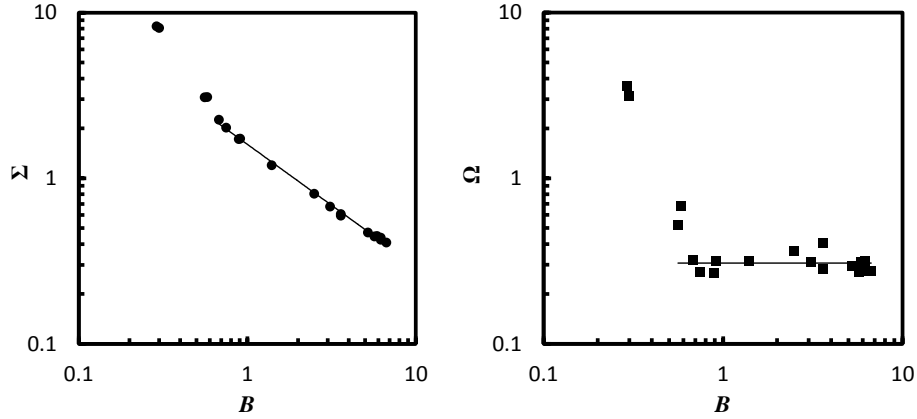


Figure 11. Dimensionless parameters fit as a function of B .

The pressure is decomposed into perturbation and static terms, $p = \tilde{p} + p_s$, where

$$\frac{dp_s}{dY} = -\rho_\infty g. \quad (3)$$

The coordinate system given in Figure 9 may be written as $Y = x \cos \theta + y \sin \theta$. Following these assumptions, the boundary layer equations,

$$\frac{\partial(\rho u)}{\partial x} + \frac{\partial(\rho v)}{\partial y} = 0 \quad (4)$$

$$\rho \left(u \frac{\partial u}{\partial x} + v \frac{\partial u}{\partial y} \right) = \frac{\partial}{\partial y} \left(\mu \frac{\partial u}{\partial y} \right) - \left(\frac{\partial \tilde{p}}{\partial x} \right)_y + (\rho_\infty - \rho) g \cos \theta \quad (5)$$

$$0 = - \left(\frac{\partial \tilde{p}}{\partial y} \right)_x + (\rho_\infty - \rho) g \sin \theta \quad (6)$$

$$\rho \left(u \frac{\partial \Phi}{\partial x} + v \frac{\partial \Phi}{\partial y} \right) = \frac{\partial}{\partial y} \left(\frac{k}{c_p} \frac{\partial \Phi}{\partial y} \right) + \dot{m}_f''' \Delta h_c \quad (7)$$

$$\rho \left(u \frac{\partial Y_i}{\partial x} + v \frac{\partial Y_i}{\partial y} \right) = \frac{\partial}{\partial y} \left(\rho D \frac{\partial Y_i}{\partial y} \right) + \dot{m}_i''' \quad (8)$$

are written for the conservation of mass, momentum, energy and species, respectively, with $\Phi = \int_{T_\infty}^T c_p dT \cong \bar{c}_p(T - T_\infty)$.

A one-step reaction is presented as the mass-based stoichiometric equation, 1 g Fuel + s g Oxygen \Rightarrow (1+s) g Product. The pressure is constant, so that the perfect gas theory gives $\rho T = \rho_\infty T_\infty$ or

$$\frac{\rho_\infty - \rho}{\rho} = \frac{T - T_\infty}{T_\infty} = \frac{\Phi}{c_p T_\infty}. \quad (9)$$

These compressible equations are transformed into an incompressible form by introducing the Howarth-Dorodnitsyn transformation [14] $z = \int_0^y \frac{\rho}{\rho_\infty} dy$, in which $z = z(x, y)$. Also, $\rho\mu$ is assumed to be constant.

The Shvab-Zel'dovich (S-Z) variables are introduced

$$\beta_{\Phi O} = \Phi + \frac{Y_o \Delta h_c}{s} \quad (10)$$

$$\beta_{\Phi F} = \Phi + Y_F \Delta h_c \quad (11)$$

$$\beta_{FO} = Y_F + \frac{Y_o}{s}. \quad (12)$$

Furthermore, the Prandtl and Schmidt number are assumed to equal unity, $Pr = \frac{\mu c_p}{k} = 1$ and $Sc = \frac{\mu}{\rho D} = 1$. A dimensionless mixture fraction is introduced,

$$\beta^* = \frac{\beta_i - \beta_{i,\infty}}{\beta_{i,w} - \beta_{i,\infty}}, \quad (13)$$

in which “w” implies conditions at the wall, $y = 0$, $z = 0$; and ∞ implies ambient conditions, where $y \rightarrow \infty$ and $z \rightarrow \infty$.

The conservation equations then become:

$$L[u] = \left(\frac{\rho_\infty - \rho}{\rho} \right) g \cos \theta - \frac{1}{\rho} \left(\frac{\partial \tilde{p}}{\partial x} \right)_y, \quad (14)$$

where the operator L is $L \equiv u \frac{\partial}{\partial x} + w \frac{\partial}{\partial z} - \frac{\partial}{\partial z} (\rho\mu) \frac{\partial}{\partial z}$ and $w = \rho v + u \int_0^y \left(\frac{\partial \rho}{\partial x} \right)_y dy$.

The pressure gradient term in Eq. (17) can be expanded by the chain rule,

$$\begin{aligned} \left(\frac{\partial \tilde{p}}{\partial x} \right)_y &= \left(\frac{\partial \tilde{p}}{\partial x} \right)_z + \left(\frac{\partial \tilde{p}}{\partial z} \right)_x \left(\frac{\partial z}{\partial x} \right)_y \\ &= -\frac{\partial}{\partial x} \int_z^\infty \left(\frac{\rho_\infty - \rho}{\rho} \right) g \sin \theta dz + \left(\frac{\rho_\infty - \rho}{\rho} \right) g \sin \theta \int_0^y \left(\frac{\partial \rho}{\partial x} \right)_y dy. \end{aligned} \quad (15)$$

Invoking slow variation of density in the x -direction allows the assumption: $\left(\frac{\partial \rho}{\partial x} \right)_y \approx 0$, and $\rho \rightarrow \bar{\rho}$, a mean density.

Then the operator over the velocity and mixture fraction becomes

$$L[u] = \left(\frac{\rho_\infty - \rho}{\rho} \right) g \cos \theta + \frac{g \sin \theta}{\bar{\rho}} \frac{\partial}{\partial x} \int_z^\infty \left(\frac{\rho_\infty - \rho}{\rho} \right) dz \quad (16)$$

with $L[\beta^*] = 0$. The second term on the left-hand side of Eq. 19, containing $\sin \theta$, is the “cross flow effect”.

The boundary conditions follow as:

$$x = 0: u = 0, \beta^* = 0$$

$$z = 0: u = 0, \quad \beta^* = 1, w = -\frac{\rho\mu}{\rho_\infty Pr} B \left(\frac{\partial \beta^*}{\partial z} \right)_{z=0}, \quad \text{where } B = \frac{\frac{Y_{o,\infty} \Delta h_c}{s} - \Phi_w}{L},$$

$$z \rightarrow \infty: u = 0, \frac{\partial u}{\partial z} = 0 \quad \text{and} \quad \beta^* = 0, \frac{\partial \beta^*}{\partial z} = 0.$$

From the relationship between density, temperature and enthalpy, along with the definition of S-Z variable it can be shown that [6, 7]

$$\frac{\rho_\infty - \rho}{\rho} = \frac{L}{\bar{c}_p T_\infty} \left[\left(B + \frac{\Phi_w}{L} \right) - B\beta^* \right] \quad 0 \leq \zeta \leq \zeta_f \quad (17)$$

$$\frac{\rho_\infty - \rho}{\rho} = \frac{L}{\bar{c}_p T_\infty} \left(\frac{B + \frac{\Phi_w}{L}}{\beta_f^*} - B \right) \beta^* \quad \zeta_f \leq \zeta \leq 1 \quad (18)$$

$$\beta_f^* = \left(\frac{B+1}{B} \right) \left(\frac{S}{S+1} \right), \zeta_f = 1 - \beta_f^{*1/3}, \quad S \equiv \frac{Y_{o,\infty}}{sY_{F,T}}, Y_{F,T} \equiv 1 \quad (19)$$

To facilitate an integral solution, the equations are integrated across the boundary layer to form ordinary differential equations

$$\frac{d}{dx} \int_0^\infty u^2 dz + \left(\frac{\mu_\infty}{\rho_\infty} \right) \left(\frac{\partial u}{\partial z} \right)_{z=0} = \int_0^\infty \left(\frac{\rho_\infty - \rho}{\rho} \right) g \cos \theta dz + \frac{g \sin \theta}{\bar{\rho}/\rho_\infty} \frac{d}{dx} \int_0^\infty z \left(\frac{\rho_\infty - \rho}{\rho} \right) dz \quad (20)$$

$$\frac{d}{dx} \int_0^\infty (u\beta^*) dz + \frac{\nu_\infty}{Pr} (B+1) \left(\frac{\partial \beta^*}{\partial z} \right)_{z=0} = 0 \quad (21)$$

in which $\frac{\rho\mu}{\rho_\infty^2} = \frac{\mu_\infty}{\rho_\infty} \equiv \nu_\infty$, the kinematic viscosity.

A new z-variable is introduced and profile functions are introduced for u and β ,

$$\int_0^\infty dz \rightarrow \delta \int_0^1 d\zeta, \zeta \equiv \frac{z}{\delta}. \quad (22)$$

The profiles satisfy the natural boundary conditions above and the derived conditions,

$$\frac{\partial^2 u}{\partial z^2} = \text{function}(x), \text{ at } z = 0$$

and

$$\frac{\partial^2 \beta}{\partial z^2} = 0 \text{ at } z \rightarrow \infty.$$

The resulting profiles follow from [6, 7],

$$u = u_0(x) \zeta (1 - \zeta)^2 \text{ and} \quad (23)$$

$$\beta^* = (1 - \zeta)^3. \quad (24)$$

Because the derived boundary condition on the velocity ignored mass transfer, a blowing correction term suggested by Marxman [15] as $\ln(1+B)/B$ was included as a multiplying term for the diffusive transport terms at the wall. The equations become

$$\begin{aligned} & \left(\int_0^1 \zeta^2 (1 - \zeta)^4 d\zeta \right) \frac{d(u_0^2 \delta)}{dx} + \gamma_\infty \frac{\ln(1+B) u_0}{B} \frac{1}{\delta} \\ & = g \cos \theta \delta \int_0^1 \left(\frac{\rho_\infty - \rho}{\rho} \right) d\zeta + \frac{g \sin \theta}{\bar{\rho}/\rho_\infty} \left[\int_0^1 \left(\frac{\rho_\infty - \rho}{\rho} \right) \zeta d\zeta \right] \frac{d(\delta^2)}{dx} \end{aligned} \quad (25)$$

and

$$\left(\int_0^1 \zeta (1 - \zeta)^5 d\zeta \right) \frac{d(u_0 \delta)}{dx} + (-3) \frac{\gamma_\infty (B+1) \ln(1+B)}{Pr} \frac{1}{\delta} \frac{1}{B} = 0. \quad (26)$$

Introducing dimensionless variables as $\xi = \frac{x}{l}$, $U = \frac{u_0 \delta}{v_\infty}$, $\Delta = \frac{\delta}{l}$ gives

$$\frac{1}{105} \frac{d(U^2 \Delta)}{d\xi} + \frac{\ln(1+B) U}{B} \frac{1}{\Delta} = \left(\frac{g \cos \theta L}{4\bar{c}_p T_\infty} \frac{l^3}{v_\infty^2} \right) \left(a \Delta + \frac{b \tan \theta}{\bar{\rho}/\rho_\infty} \frac{d\Delta^2}{d\xi} \right) \quad (27)$$

$$\frac{1}{42} \frac{d(U \Delta)}{d\xi} - \frac{3(B+1) \ln(1+B)}{Pr} \frac{1}{B \Delta} = 0 \quad (28)$$

with

$$a \equiv 3(B + \tau_0) \zeta_f + \tau_0, \quad (29a)$$

and

$$b \equiv \left(\frac{B + \tau_0}{S} \right) (6\zeta_f^2 + 3\zeta_f + 1) - \frac{B}{5}, \tau_0 = \frac{\Phi_w}{L} = \frac{\bar{c}_p (T_w - T_\infty)}{L}. \quad (29b)$$

Using initial condition $\xi = 0, U = \Delta = 0$, solutions for U and Δ with regard to ξ can be found. The term containing b above is the cross flow effect. When $b = 0$, the analytical solutions given in Eq. (1) and (2) can be found, otherwise a numerical solution must be rendered.

The burning rate and the flame standoff distance can be formulated as follows:

The local burning rate is

$$\frac{\dot{m}_F'' l}{\mu_\infty} = \frac{3 \ln(1+B)}{Pr \Delta}, \quad (30)$$

the average burning rate is

$$\frac{\bar{m}_F'' l}{\mu_\infty} = \frac{3}{Pr} \ln(1+B) \int_0^1 \frac{d\xi}{\Delta} \quad (31)$$

and the flame standoff distance is

$$y_f = c \Delta l, \text{ with } c \equiv \left(\frac{L}{4\bar{c}_p T_\infty} \right) \left[4(B + \tau_0) \zeta_f + B \left[(1 - \zeta_f)^4 - 1 \right] \right] + \zeta_f. \quad (32)$$

For $b = 0$, by which the cross-flow effect is neglected, the equations are solved analytically as done previously by Ahmad and Faeth [6, 7] giving

$$U = \left[\frac{168a(1+B)Gr_l^*}{2(1+B) + Pr} \right]^{\frac{1}{2}} \xi^{\frac{1}{2}} \quad (33)$$

$$\Delta = \left[\frac{\ln(1+B)}{BPr} \right]^{\frac{1}{2}} \left[\frac{168(1+B)[2(1+B) + Pr]}{Gr_l^* a} \right]^{\frac{1}{4}} \xi^{\frac{1}{4}} \quad (34)$$

$$\text{in which } Gr_l^* = \frac{g \cos \theta L}{4\bar{c}_p T_\infty} \frac{l^3}{v_\infty^2}.$$

Substituting U and Δ into the burning rate and flame standoff distance gives Eqns. (1) and (2).

For the b term not equal to zero, the equations are solved numerically using *Mathematica*. Due to singularity issues near the origin, the solution was problematic and is only solved for limited cases. The results of the experiments will be compared to solutions with and without the cross flow term.

Figure 11 shows the results of the theory compared to methanol data of 10 cm in length. Little difference is found from the theoretical result with and without the cross flow effect. Also, the results vary little with angle, and the flame standoff distance is again over-predicted, especially for burning on the underside. Moreover, the steady laminar theory does not fully apply.

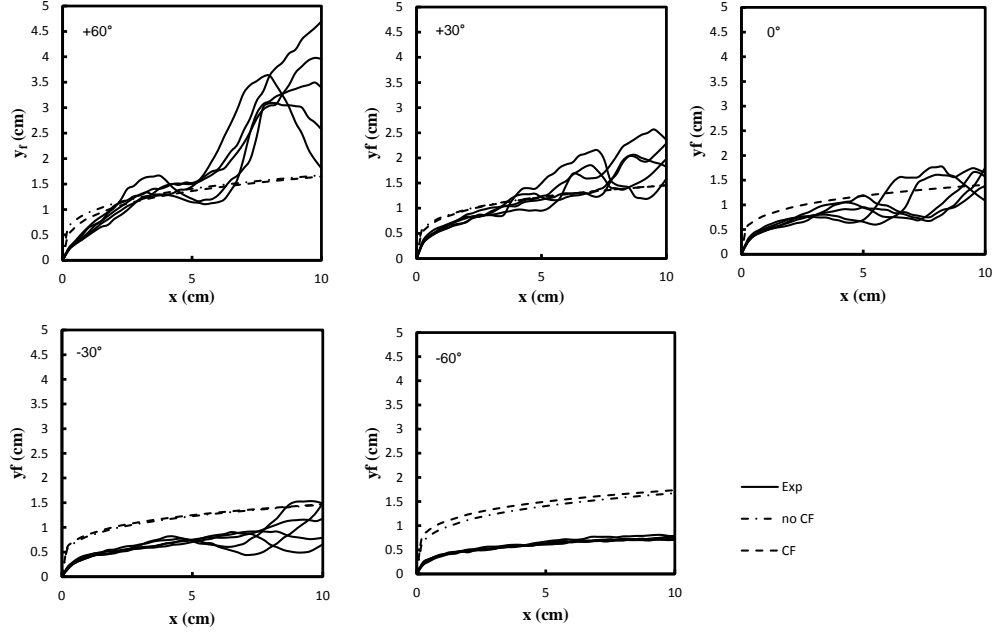


Figure 11. Comparison of theoretical and experimental instantaneous results for flame standoff with methanol of $l = 10$ cm

Figure 12 shows the burning rate per unit area results for ethanol and methanol. The burning rate is higher for top burning at corresponding orientations than burning on the underside with the cross flow term (CF) included. Without CF, the results are symmetrical. The CF results better agree with the data of Figure 6, and support the increase in burning rate with angle as depicted in Figure 10.

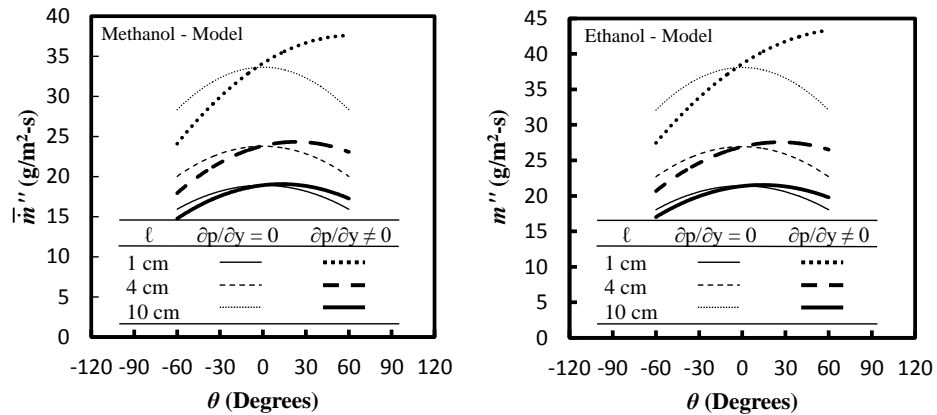


Figure 12. Theoretical results for average burning flux for methanol and ethanol

CONCLUSIONS

Measurements of flame location and burning rate were recorded for flat plate wicks of methanol and ethanol, ranging in size from 1 to 10 cm, and oriented from 0° (vertical) to +/- 90° (top/bottom). The dimensionless laminar correlations of Ahmad and Faeth [6, 7] roughly support the data for flame location and burning flux, however the flame location is over predicted, and indicates no additional dependence on the angle. In contrast, the results for the burning rate indicate increasing rates with angle. In addition, there is a maximum burning rate at + 30° whose location with angle appears to decrease as the length of the plate increases. While the theory only considers laminar steady pure convection, issues related to the onset of turbulence and radiation is present. The inclusion of the cross flow, or normal pressure term, in the theory gives improved results, especially in predicting the differences in the top and bottom burning rate for the same plate orientation. Simple fits for mass burning rates and flame standoff, equations (2f) and (2g) were formed based on the theory which include dependence on the Grashof number, B number and angle.

ACKNOWLEDGMENTS

The authors would like to thank M. Huis, M. Lutz, and M. Willnauer for their contributions. This work was supported by a NASA Office of the Chief Technologist's Space Technology Research Fellowship (NASA Grant NNX11AN68H with grant monitor D. Urban). This work was also funded by NASA Grant NNX10AD98G, with P. Ferkul as technical contact.

REFERENCES

1. Blackshear Jr., P.L. and Murty, K.A., "Heat and mass transfer to, from, and within cellulosic solids burning in air," Symposium (Intl.) on Combustion 10: 911-923 (1965).
2. Blackshear Jr., P.L. and Murty, K.A., "Some effects of size, orientation, and fuel molecular weight on the burning of fuel-soaked wicks," Symposium (Intl.) on Combustion 11: 545-552 (1967).
3. Kosdon, F.J., Williams, F.A. and Buman, C., "Combustion of vertical cellulosic cylinders in air," Symposium (Intl.) on Combustion 12: 254-264 (1969).
4. Kim, J.S, de Ris, J. and Kroesser, William F., "Laminar free-convective burning of fuel surfaces," Symposium (Intl.) on Combustion 13: 949-961 (1971).
5. Orloff, L. and de Ris, J., "Modeling of Ceiling Fires," Symposium (Intl.) on Combustion 13: 979-992 (1971).
6. Ahmad, T. and Faeth, G.M., "Turbulent wall fires," Symposium (Intl.) on Combustion 17: 1149-1160 (1979).
7. Ahmad, T., "Investigation of the Combusting Region of Fire-Induced Plumes Along Upright Surfaces," Ph.D. Thesis, The Pennsylvania State University, 1978.
8. Ali, S., Raghavan, V. and Rangwala, A., "A numerical study of quasi-steady burning characteristics of a condensed fuel: effect of angular orientation of fuel surface," Combustion Theory and Modeling 14, No. 4: 495-518 (2010).
9. Ohtani, H., Ohta, K. and Uehara, Y., "Effect of orientation on burning rate of solid combustible," Fire and Materials 18: 191-193 (1991).
10. Gollner, M.J., Huang, X., Cobian, J., Rangwala, A.S. and Williams, F.A., "Experimental study of upward flame spread of an inclined fuel surface," Proceedings of the Combustion Institute 34: 2531-2538 (2013).
11. Lloyd J.R., Sparrow E.M., "On the Instability of natural convection flow on inclined plates," Journal of Fluid Mechanics, No. 42, pp. 465-470 (1970).
12. Al-Arabi, M. and Sakr, B., "Natural convection heat transfer from inclined isothermal plates," International Journal of heat and Mass Transfer, 31: 559-566 (1988).
13. Bustamante, M., "Experimental Investigation Of Liquid And Gas Fueled Flames Towards The Development Of A Burning Rate Emulator (BRE) For Microgravity Applications", Master of Science Thesis, Dept. of Fire Protection Engineering, University of Maryland, College Park, MD 20742, 2012.
14. Howarth, L., "Concerning the effect compressibility on laminar boundary layers and their separation," Proc. Roy. Soc. London Ser. A 194: 16-42 (1948).
15. Marxman, G., Gilbert, M., "Combustion in the Turbulent Boundary Layer on a Vaporization Surface," Symposium (Intl.) on Combustion 10: 1337-1349 (1965).
16. Quintiere, J.G., *Fundamentals of Fire Phenomena*. John Wiley & Sons Ltd., Chichester, UK, 2006.

8th U. S. National Combustion Meeting
Organized by the Western States Section of the Combustion Institute
and hosted by the University of Utah
May 19-22, 2013

A Burning Rate Emulator for Study in Microgravity

Y. Zhang, M.J. Bustamante, P.B. Sunderland, J.G. Quintiere¹

P. Ferkul²

¹*Dept. of Fire Protection Engineering, University of Maryland, College Park, MD 20742, USA*
²*NCSEER, Cleveland, OH 44135*

A gas-fueled burner with embedded heat flux gages has been used to emulate the burning characteristics of several liquid and solid fuels. Dubbed the Burning Rate Emulator (BRE), it establishes the heat of gasification (L) in steady burning by measurements of surface temperature, incident flame heat flux, and flow rate of a gaseous fuel mixture. The mixture is selected with appropriate properties such as the heat of combustion and radiation character by the soot point. Results are shown to accurately emulate methanol, heptane, and PMMA pool fires of 50 mm in diameter. Used in a microgravity environment, a BRE can readily identify stable and steady burning conditions yielding relevant fuel properties: heat of gasification, surface temperature, heat of combustion, and smoke point. These properties identify a potential real condensed-phase fuel that can burn in microgravity. Repeated experiments identify a range of fuel conditions that can support microgravity burning. The flammability region is bounded by extinction values, and critical conditions needed for ignition can also be established. The plausibility of the BRE has been demonstrated for normal gravity conditions, and a burner without heat-flux sensors has achieved an appearance of steady burning in the NASA 2.2-s drop tower. Recent tests with a 50-mm-diameter burner including heat flux measurements conducted in a 5.18-s drop facility have indicated stable flames with ethylene.

1. Introduction

This study seeks to establish the burning conditions for condensed fuels in a quiescent environment. The burning conditions represent those of steady burning with the heat of gasification of the material as the principal fuel property. In addition, the heat of combustion controlling flame extent, surface re-radiation heat flux, and flame radiation properties will influence the burning rate. We seek to define the burning in terms of these properties by using an emulator having a controlled gaseous fuel supply to simulate steady burning of material with those properties. The burning rate emulator (BRE) can be operated to represent a range of real solid and liquid fuels, and can also simulate an applied external heat flux when considering an effective heat of gasification.

Steady burning (rate per unit area or fuel flux) can be expressed as

$$\dot{m}'' = \frac{\dot{q}_f'' - \dot{q}_{rr}'' + \dot{q}_e''}{L} \quad (1)$$

where \dot{q}_f'' is the incident flame heat flux, \dot{q}_{rr}'' is the surface radiative loss heat flux to ambient, \dot{q}_e'' is the incident external radiative heat flux, and L is the heat of gasification. The heat of gasification is defined precisely for liquids as

$$L = h_{vap} + c_p(T_v - T_\infty), \quad (2)$$

where h_{vap} is the heat of vaporization, c_p is the specific heat, T_v is the surface vaporization temperature, and T_∞ is the ambient temperature.

The flame heat flux is controlled by diffusive and radiative components, and the surface re-radiation heat flux by the temperature of the vaporizing surface. In the case of the emulator burner (BRE), it is the burner surface temperature that gives the surface re-radiation. Heat flux gages in the surface record the flame heat flux distribution. With the measured gas flow rate of the burner, values of L , with and without an external heat source, can be determined from Eq. (1). By varying the gaseous fuel, the heat of combustion and the radiation character (notably the smoke point) can be varied. For a given configuration, a wide range of burning conditions can be readily established with the emulator (BRE). The long term goal is to use BRE to study the microgravity burning behavior of the condensed fuel. However, here we will mainly focus on establishing the feasibility of the emulator and sharing preliminary results in drop tower testing.

2. Background

Orloff (1971) and de Ris, de Ris et al. (1975) and Kim et al. (1971) pioneered the use of sintered metal burners for studying the burning of planar condensed-phase steady burning. As with the Brahmi et al. (2005) burner, the flow of the fuel is distributed uniformly over the burner. This uniform flow is in contrast to the actual flow velocity of the supplied vapor that is governed by the local heat transfer from the flame. As the flame shape changes, so does the vapor velocity. Nevertheless, de Ris and co-workers successfully simulated burning conditions for a wide range of B numbers. The B number is defined as

$$B \equiv \frac{Y_{ox}\Delta h_c / r - c_p(T_v - T_\infty)}{L} \quad (3)$$

where Y_{ox} is the ambient oxygen mass fraction, Δh_c is the heat of combustion, r is the stoichiometric oxygen to fuel ratio, c_p is the specific heat of gas mixture, T_v is the surface vaporization temperature, and T_∞ is the ambient temperature.

For a given ambient condition, the B number is principally a function of the heat of gasification, L . The burning rate per unit area is also principally a function of the B number in purely diffusive or convective burning. Flame radiation and surface re-radiation perturb this simple dependence. However, the relatively simple dependence could be emulated by the de Ris burner, and is shown to follow laminar flame theory. Thus, despite the imperfection of a uniform burner velocity, the results yielded theoretically supported results for burning and flame shape.

In the de Ris burner, the heat of gasification was determined by Eq. (1) with no external radiation and negligible re-radiation. The latter was accomplished by flowing water through the burner's sintered metal matrix. An energy balance on the water, after considerable time to achieve thermal equilibrium of the burner, allowed an average flame heat flux to be determined. Nitrogen addition to the gaseous fuel also allowed for variations in the supplied fuel mixture mass flux.

Another proof of burner emulation was demonstrated by Bustamante et al. (2012) by comparing the flame standoff distance in the laminar region for burning of inclined flat plates. A pure methane flame was used in a porous plate burner and compared to a methanol flame on a fuel-soaked wick plate. Results showed the similarity in the flame shape along the surface oriented at different angles from a ceiling fire, to a vertical wall fire, to a pool fire. Also the onset of transition to turbulent flow was matched. The paper noted a difference of fire size in the turbulent over-fire region due to a mismatch between the heats combustion of methane and methanol.

3. Experimental Method

A BRE burner has been designed and constructed, inspired by the de Ris burner. Its size has been selected based on our flight and drop tower tests, and the burner size used by Brahmi et al (2005). The BRE burner has a face of 50 mm in diameter. Owing to the anticipated heat flux variation over the surface while burning in microgravity or normal gravity, two sensors are used. An appropriate averaging of the two heat fluxes provides the needed average heat flux for computing the heat of gasification. The thermocouples at the operating face record the surface temperature, allowing the re-radiation heat flux to be estimated. Glass beads provide a porous matrix for fuel flow, ensuring a uniform fuel flux, and porous brass screen serves as its face and internal layers. Figure 1 shows the BRE burner with heat flux sensors at the center and near the edge.

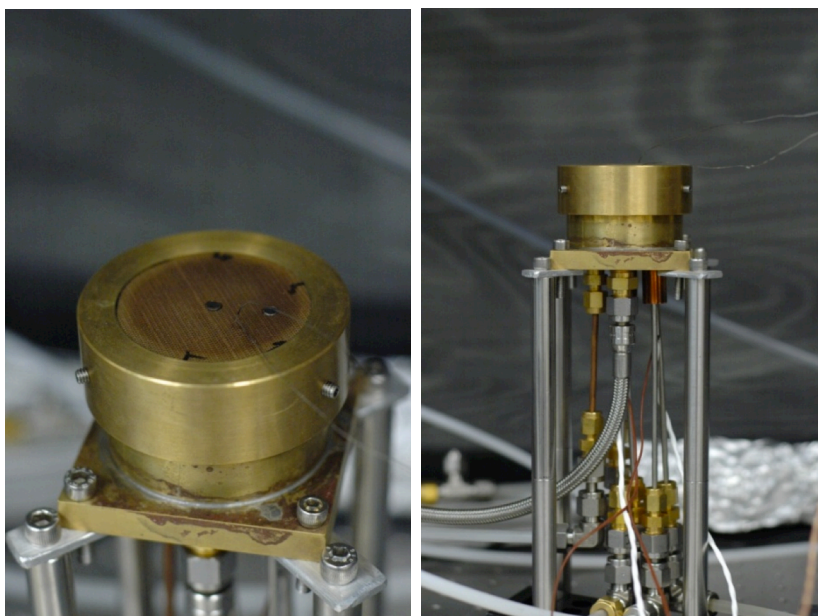


Figure 1. BRE burner with 50 mm diameter surface.

Validation in 1-g. A series of tests were performed to assess burner's ability to emulate condensed-fuel combustion. It was reasoned that fuel properties that control the burning rate are (1) the heat of combustion, especially controlling flame height; (2) the heat of gasification, an approximation to evaporative condensed-phase fuels; (3) the surface temperature or corresponding re-radiation; and (4) the smoke point, which determines flame radiation. These properties must reasonably match those of the condensed fuel of interest.

The burning rate of the condensed fuel is determined by a load-cell measurement of a pool fire. Then literature values are established for the four fuel properties as described above. Two of the four properties – heat of combustion and smoke point – are matched by selecting the proper gaseous fuel.

The other two properties – heat of gasification and surface temperature – indicate the burning condition. We wish to match these properties with a gaseous fuel mixture having the same mixture flow rate as the pool fire to evaluate the concept of BRE.

We tested the BRE to see if it could emulate a 50 mm pool of methanol burning steadily. The mass loss rate of methanol was measured and the flame was photographed. To match the methanol with the BRE we would need to use a gaseous fuel with the same flow rate. To match the flame height and consequently the heat flux, the fuel must have the same heat of combustion. In addition, consideration of the sooting tendency led to the choice of methane as the gaseous fuel. Nitrogen was added to the fuel stream to match the heat of combustion of methanol, 19.1 kJ/g (Tewarson, 2002). The gas burner BRE used a fuel mixture of 52% (volume) methane with 48% nitrogen. The flow rate of the mixture was 33 cc/s to match the burning rate of the methanol, 11 g/m²-s.

If the BRE concept is correct, the two flames should be nearly identical in appearance and heat flux distribution. The measured heat fluxes in the BRE are 5.5 and 21.3 kW/m² for the heat flux gages located at the center and at 1.5 cm from the center, respectively. A weighted average over their area segments gives an average value of 15.6 kW/m². Corresponding surface temperature measurements yield an average temperature of 160 °C (141 – 170 °C). Assuming an emissivity of unity for the oxidized porous brass surface, the re-radiative heat flux is 2 kW/m². Consequently, the heat of gasification associated with the BRE is computed from Eq. (1) as $L = (15.6 - 2 \text{ kW/m}^2) / (11 \text{ g/m}^2\text{-s}) = 1.24 \text{ kJ/g}$. The literature value for methanol is 1.20 kJ/g (Quintiere, 2006). Besides the approximations in the calculations, the slight difference possibly arises because the BRE surface is hotter than the boiling point of methanol, 64 °C. The visual confirmation of the BRE to emulate the methanol pool fire at 50 mm diameter is shown in Fig. 2a and 2b, in which the flames are compared when the slightly oscillating images are similar.

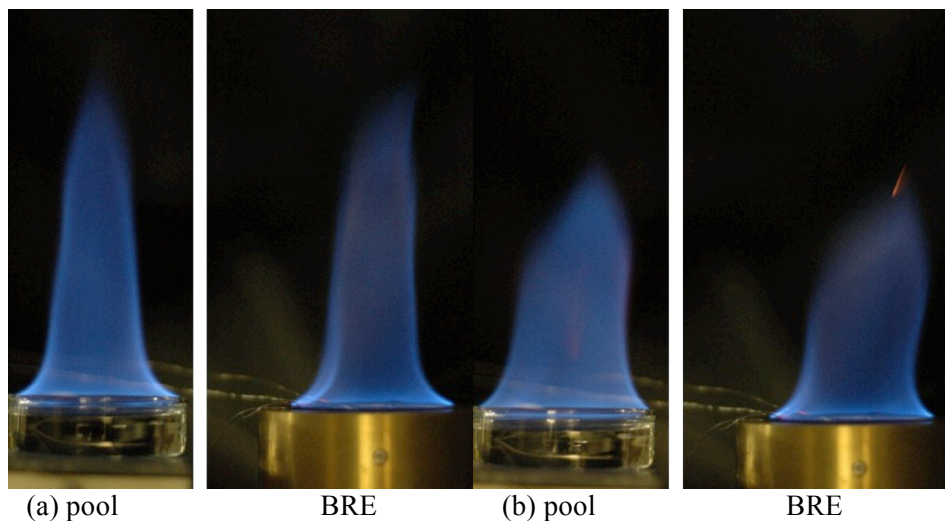


Figure 2. Comparison of 50 mm diameter methanol flame reproduced by the BRE burner.

We sought to evaluate whether the burner could also emulate other burning conditions. We considered a 50-mm-diameter burning pool of heptane and PMMA. The choice of the gaseous fuels was similar to that of methanol. Ethylene was selected to be used as the burner gas to simulate heptane. The heat of combustion of ethylene is close to that of heptane (41.5 kJ/g compared to 41.2 kJ/g), as is the smoke point (120 mm compared to 139 mm) (Li and Sunderland, 2012). The gas burner BRE used pure ethylene with 26.5 cc/s flow rate to match the measured burning rate of the heptane of 15

$\text{g/m}^2\text{-s}$. A visual confirmation for the nature of these turbulent flames is shown in Fig. 3.

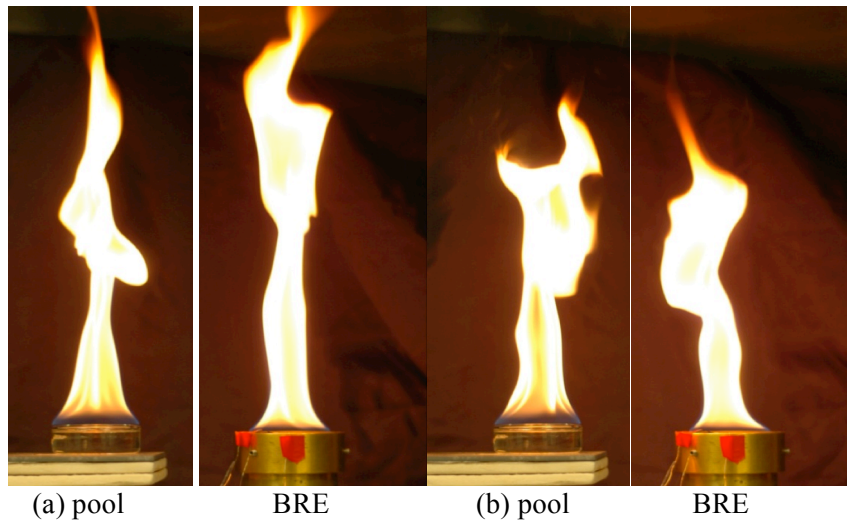


Figure 3. Comparison of 50 mm diameter heptane flame reproduced by the BRE burner.

Propylene and nitrogen (50% in mole fraction) were used to emulate PMMA. The resulting gas mixture had a similar heat of combustion and smoke point as those of PMMA (24.3 kJ/g compared to 24.2 kJ/g, smoke point is 105 mm compared to 116.6 mm). Steady burning of the PMMA was achieved by igniting it in an inverted orientation (facing down) and allowing the flame to stabilize, after which the sample was oriented as a pool fire where it sustained steady burning. The fuel flow rate was matched to the mass-loss rate of $6.36 \text{ g/m}^2\text{-s}$. A visual confirmation for the comparison of PMMA and BRE is shown in Fig. 4.

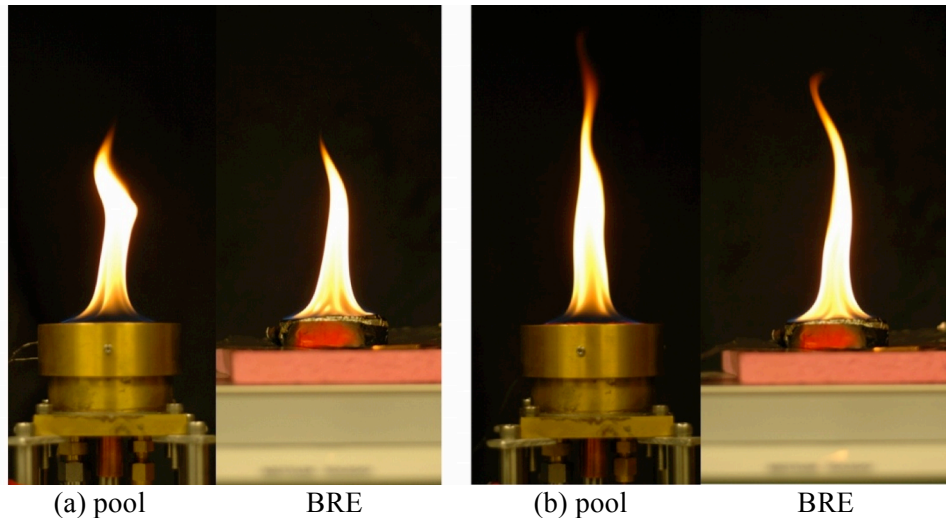


Figure 4. Comparison of 50 mm diameter PMMA flame reproduced by the BRE burner.

Table 1. The literature and measured properties that determine the burning conditions

		Δh_c (kJ/g)	Smoke Point (mm)	T_s (°C)	L (kJ/g)
Methanol	Pool	19	-	65	1.24
	BRE ($X_{CH_4}=52\%$, $X_{N_2}=48\%$)	19	-	160	1.2
Heptane	Pool	41.2	139	98	0.48
	BRE (C_2H_4)	41.5	120	211	0.51
PMMA	Pool	24.2	105	270	1.6
	BRE ($X_{C_3H_6}=50\%$, $X_{N_2}=50\%$)	24.3	116.6	312	1.8

4. Applications of the BRE

Having demonstrated the BRE's capability to emulate the combustion of various fuels in normal gravity, extensions of its use can be considered. In addition to steady burning, the conditions of ignition and extinction can be examined relative to condensed-phase fuels. By the determination of these conditions, a mapping of the properties that allow burning with boundaries of ignition and extinction can be produced. This conceivably can be done in normal as well as microgravity. Moreover the conditions of burning can be efficiently established in microgravity using the BRE. Some preliminary results in this regard are examined below.

Conditions at ignition or extinction. Mass-loss flux at ignition and extinction limits are important properties of fires. Yet their evaluation for materials is difficult to capture with current experimental methods. Materials experience a sudden jump in mass-loss rate when ignited or when they suddenly extinguish. Such transients are difficult to accurately measure. By using the BRE, the mass-loss rate could be clearly identified by increasing the flow rate of fuel gradually until the establishment of the flame is observed, or decreasing it after a flame is sustained.

A theoretical analysis for extinction can be put forth based on the relationship for steady burning, and its ability to exceed a critical flame temperature for the flame to survive. A critical temperature needed for the survival of a diffusion flame can be taken as 1300 °C (Quintiere and Rangwala, 2004). This temperature is a reasonable criterion for the extinction of a laminar flame under its environmental conditions, including gravity effects. Following B-number theory for pure convective burning, and considering a small B number as would occur near extinction, we write:

$$\dot{m}'' L_m = \frac{h_c}{c_p} \left[Y_{ox} (1 - X_r) \Delta h_c / r - c_p (T_v - T_\infty) \right] \quad (4)$$

$$L_m \equiv L - \frac{\dot{q}_{f,r}'' + \dot{q}_e'' - \dot{q}_{rr}''}{\dot{m}''} \quad (5)$$

where L_m is an effective heat of gasification, h_c is the convective heat transfer coefficient, and X_r is the flame radiation loss fraction.

The flame temperature (T_f) can be determined e.g. Quintiere (2006):

$$c_p (T_f - T_\infty) = \frac{Y_{F,o} (1 - X_r) \Delta h_c - L_m + c_p (T_v - T_\infty)}{1 + r Y_{F,o} / Y_{ox}} \quad (6)$$

These equations, (4), (5) and (6), can be combined by eliminating L_m to yield:

$$\dot{m}'' \Delta h_c = \frac{\frac{h_c}{c_p} [(1 - X_r) \Delta h_\infty - c_p (T_v - T_\infty)]}{Y_{F,o} (1 - X_r) + \frac{c_p (T_v - T_\infty) Y_{ox}}{\Delta h_\infty} - \frac{c_p (T_f - T_\infty)}{\Delta h_\infty} \left(\frac{Y_{ox}}{r} + Y_{F,o} \right)} \quad (7)$$

where Δh_∞ is the heat of combustion per unit ambient oxidizer, $\frac{Y_{ox} \Delta h_c}{r}$. This theory is presented for an h_c of 14 W/m²-K in Fig.5 along with extinction data taken in the 50 mm BRE for various gaseous fuels. Also plotted are data from Lyon et al. (2007) for actual solid fuels. The theory does not collapse onto a single curve for the various fuels used, perhaps due to the neglect of radiation.

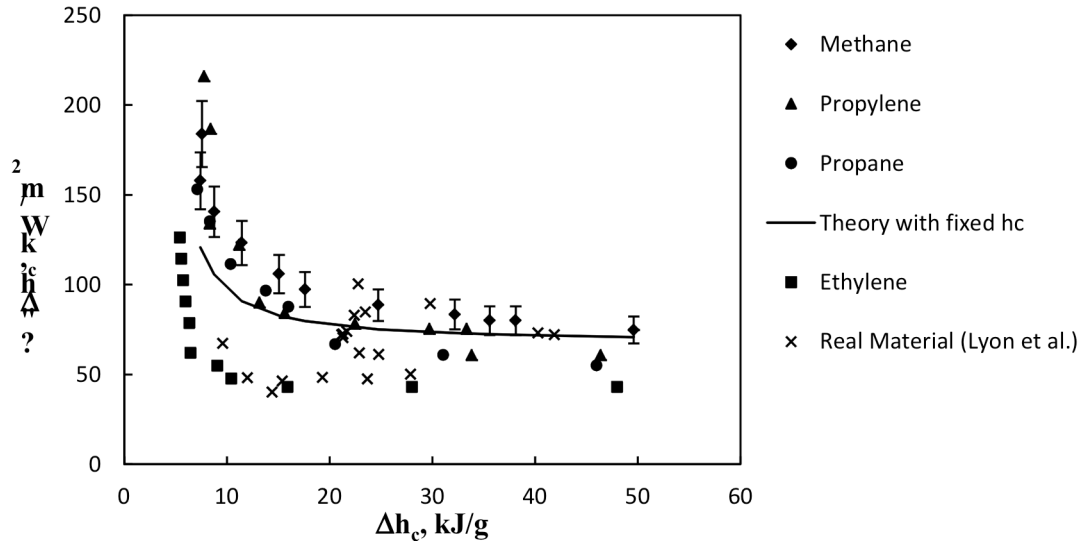


Figure 5. Extinction conditions for various solid fuels and data from the BRE for several gaseous fuels

Flammability Map. The BRE can be used for various fuels, and their selection prescribes the heat of combustion and smoke point. Over a range of flow rates where a steady flame is sustained, the BRE establishes the corresponding heat of gasification and burning temperature. These burning points can be plotted in a three-dimensional graph with coordinates of heat of combustion, heat of gasification, and re-radiation heat flux -- all fuel properties that allow steady burning. Many of these points may correspond to fictitious condensed-phase fuels. Some preliminary results for normal gravity conditions are displayed in Fig. 6.

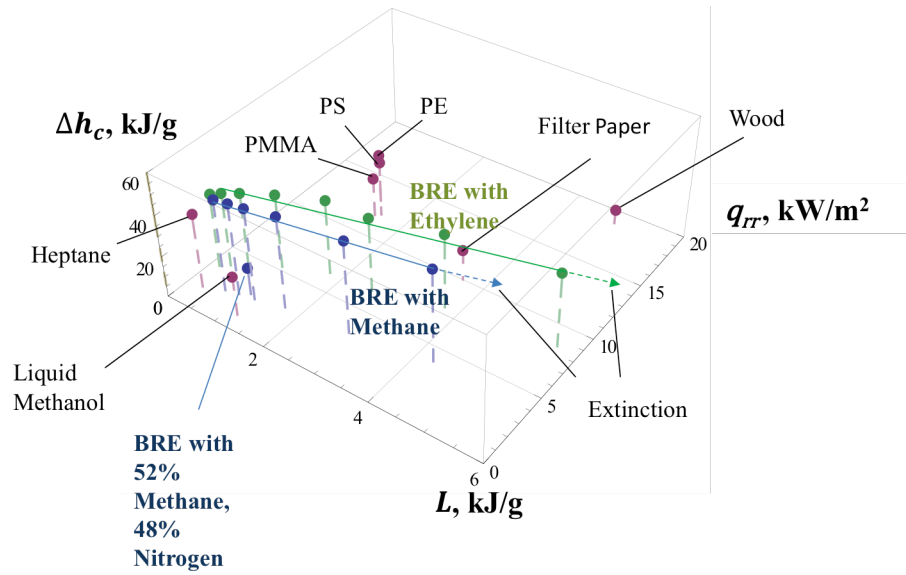


Figure 6. Flammability map by BRE in normal gravity

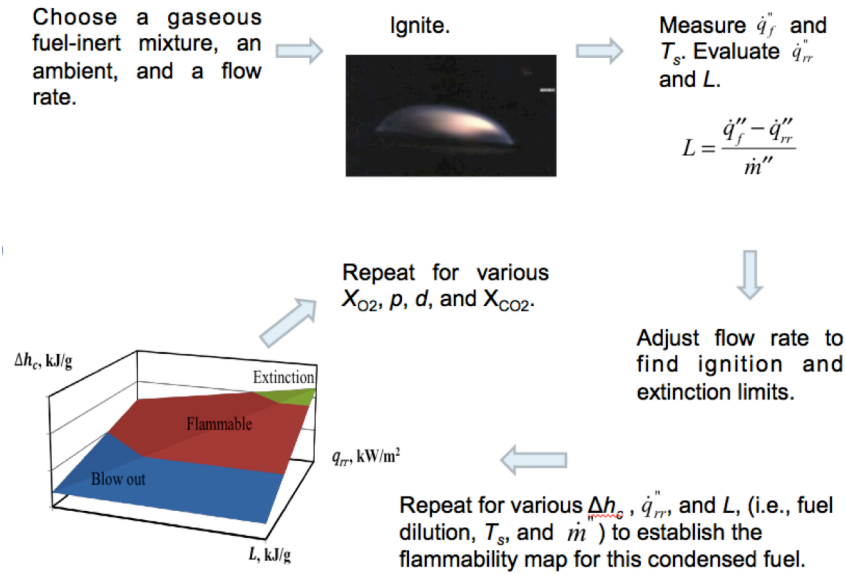


Figure 7. Illustration of the process in establishing a microgravity flammability map

Burning behavior is different in microgravity. However, the fuel fire properties, such as the heat of gasification, remain the same. One can identify a fuel that burns in microgravity using the BRE consistent with the heat of gasification and other fuel properties. By changing the heat of combustion (via the type of fuel or its diluent concentration) and fuel flow rate, diverse burning conditions can be identified in microgravity. This can yield a flammability map with respect to the heat of gasification, which could be directly associated with a specific condensed fuel. This would provide a better method to evaluate material flammability in microgravity than the current NASA flame spread test, conducted in normal gravity. Other important burning behaviors, like the flame heat flux and

burning rate, could also be explored in microgravity with the BRE. The process is illustrated in Fig. 7.

Burning in Microgravity. Of course we have little evidence that condensed phase fuels can steadily burn in microgravity conditions. Here we put forth an approximate analysis to estimate the possibility for fuel to burn in microgravity.

Let us ignore the addition of external radiation and estimate what materials are likely to burn in microgravity. As it would be difficult to estimate, the flame radiation is neglected here where it is likely to be small in microgravity. Consequently, we apply Eq. (4) ignoring the small heat capacity term, as

$$\dot{m}''L \approx \frac{h_c}{c_p} \Delta h_\infty - \dot{q}_{rr}'' . \quad (8)$$

The convective heat transfer coefficient must be estimated for microgravity. We treat this as pure conduction, from a flame whose standoff distance is estimated from the low-*Re* jet study of Sunderland et al. (1999). We choose a coefficient corresponding to methane, $C_f = 0.192$, and a diameter corresponding to our prototype burner, $d = 50$ mm. In terms of the burning flux, the flame standoff is given as

$$\delta = \frac{C_f d^2 \dot{m}''}{\mu} \quad (9)$$

where μ is the fuel viscosity. The convective coefficient is given as

$$h_c \approx \frac{k}{\delta} \quad (10)$$

where k is the conductivity of the fuel. The following property selections are made:

$$\begin{aligned} k &= 0.0257 \text{ W/m-K} \\ m &= nr = (15 \times 10^{-6} \text{ m}^2/\text{s}) (1.2 \text{ kg/m}^3) \\ c_p &= 1.0 \text{ kJ/kg-K} \\ \text{and} \\ d &= 50 \text{ mm.} \end{aligned}$$

Consequently $\frac{h_c}{c_p} \approx \frac{1 \cdot (\text{g/m}^2/\text{s})^2}{\dot{m}''}$. Equation (8) now becomes

$$\dot{m}''^2 L + \dot{q}_{rr}'' \dot{m}'' - \Delta h_\infty \approx 0 . \quad (11)$$

Eq. (11) estimates the burning flux for a planar material of diameter 50 mm burning in microgravity. Larger sizes reduce the convective coefficient by $1/d^2$, and lower the burning flux. A simpler form of the extinction equation (7) is used to estimate the extinction conditions in microgravity, i.e., let $Y_{F,o} = 1$ and

$\Delta h_{\infty} \approx 3 \text{ kJ/g}$ for ambient air,

$$\frac{Y_{ox}}{r} \approx 0.1 \text{ to } 0.3,$$

$$\frac{c_p (T_v - T_{\infty})}{\Delta h_{\infty}} \approx 0.1,$$

$$\frac{c_p (T_f - T_{\infty})}{\Delta h_{\infty}} \approx 0.4, \text{ at extinction.}$$

Eq. (7) can be approximately represented at extinction as

$$\dot{m}_{crit}'' \Delta h_c \approx \frac{\frac{h_c}{c_p} [(1 - X_r) \Delta h_{\infty} - c_p (T_v - T_{\infty})]}{0.5} \quad (12)$$

Combining Eq. (11) with Eq. (4) at extinction, and recognizing that flame radiation will be small at extinction, a criterion for steady burning is established as

$$\dot{m}_{crit}'' = \frac{\dot{q}_{rr}'' - \dot{q}_e''}{(\Delta h_c / 2) - L}. \quad (13)$$

Materials cannot have burning rates below this critical value. Note that the addition of external radiant heating will reduce the critical burning flux.

Let us select representative properties for liquid fuels, thermoplastics, high-temperature polymers, and halogenated polymers. Table 2 gives generic properties, the results of computing the mass flux estimated for burning in microgravity, and the critical mass flux. It is seen from the table that generic liquid fuels would burn in microgravity, while ordinary polymers are marginal, and high-temperature and halogenated polymers would not burn. Of course, the addition of external radiation would mitigate the situation and allow all fuels to burn.

Table 2. Estimated burning conditions in microgravity for a planar material of 50 mm diameter.

Parameter	Liquids	Thermoplastics	High-temperature Polymer	Halogenated Polymer
Heat of Combustion, kJ/g	30	30	15	8
Heat of Gasification, kJ/g	0.5	3	5	3
Re-radiation Flux, kW/m ²	0.5	10	20	30
Burning Flux, g/m ² s	2	0.5	0.1	0.2
Critical burn flux, g/m ² s	0.03	0.8	8	29

5. Drop Tower Results

For some conditions, preliminary NASA testing (Takahashi et al., 2012) in a 2s drop tower indicated a trend toward stable flames for a burner without heat flux sensors to measure the flame thermal feedback. Encouraged by these tests, the BRE 50 mm burner was used in the NASA 5 s drop facility. The burner surface temperatures were also recorded, but the face temperature of the thermopile heat flux gages were allowed to achieve their equilibrium; they were not measured or controlled by 65°C water as in ground tests. The current results are summarized in Fig. 8 showing the nature of the flame under several flow conditions for pure ethylene. The photos were taken from video records at

the end of the drop. They show the side and top views for ethylene flow rate of 135 to 300 ccm. At 90 ccm, the flame was unstable and near extinction. At the higher flows, the flames appeared to be stabilizing, and heat flux appeared to be asymptotically approaching steady state. Longer duration tests, like those planned for the International Space Station, would confirm whether these are truly steady flames.

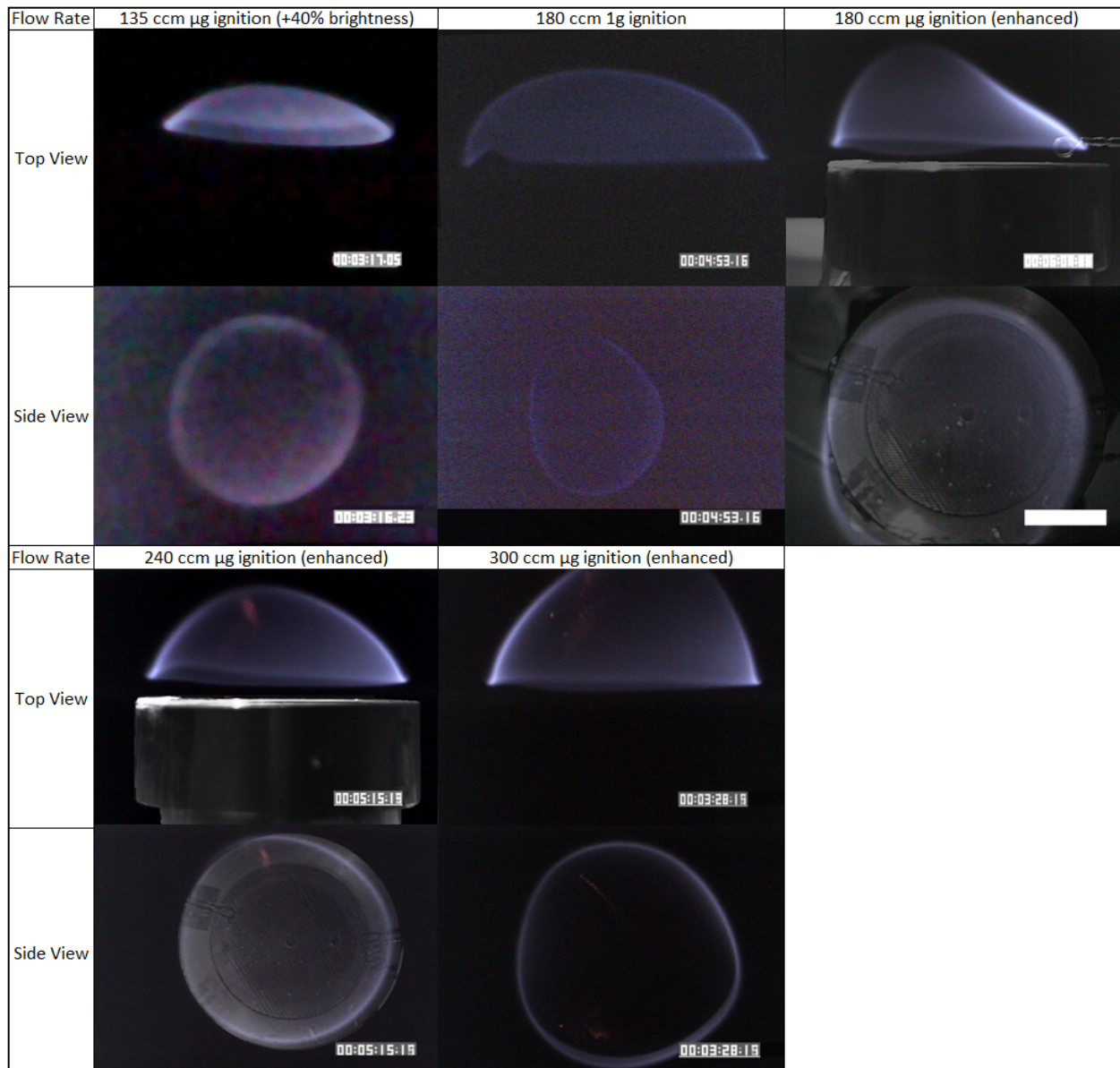


Figure 8. Photos at the end of the drop for ethylene flames in the 50 mm BRE at flow rates from 135 to 300 ccm

Assuming that the photos display steady flames, the temperature and heat flux data can be interpreted to yield corresponding heats of gasification for each flow rate. The results, along with other fuel properties, are summarized in Table 3. It is interesting to observe that the heat of gasification, corresponding to the burner temperature and heat flux, drops as the burning flux increases. This trend is shown more clearly in Fig. 9.

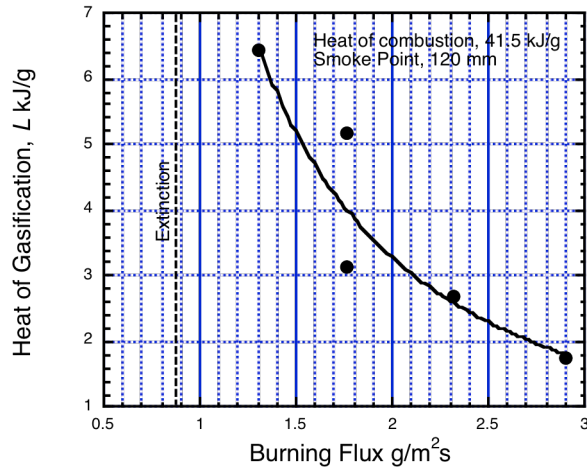


Figure 9. Heats of gasification at quasi-steady μg burning

The results in Fig. 9 suggest that fires of 50 mm in diameter with liquid fuels having typical L values of about 1 kJ/g or less and some plastic materials having high heats of combustion are likely to sustain microgravity burning. However, the ignition of such solids can be problematic in microgravity, as recalling the procedure we used to sustain the burning of PMMA in normal gravity. These drop test results are somewhat in accord with the estimates for burning of Table 2, suggesting the ease of burning some liquid fuel in microgravity.

Table 3. Summary of 5 s drop tower burning conditions at the end of the drop

Test No.	D9023	D9024	D9027	D9028	D9029	D9030
	(Extinguished)					
Fuel	C_2H_4	C_2H_4	C_2H_4	C_2H_4	C_2H_4	C_2H_4
Heat of Combustion (kJ/g)	41.5	41.5	41.5	41.5	41.5	41.5
Smoke Point (mm)	120	120	120	120	120	120
Ignition	1g	1g	μg	μg	μg	μg
Fuel Rate (ccm)	180	90	180	135	240	300
Burning Rate ($\text{g}/\text{m}^2\text{-s}$)	1.76	0.88	1.76	1.3	2.32	2.9
HF_Center (kW/m^2)	5.68		5.68	5.68	4.27	3.6
HF_Edge (kW/m^2)	7.08		10	9.19	6.8	5.65
Average HF (kW/m^2)	6.85		9.29	8.61	6.38	5.31
Center T_s ($^{\circ}\text{C}$)	133		60	66	52	48
Outer T_s ($^{\circ}\text{C}$)	150		55	60	56	54
Averaged T_s ($^{\circ}\text{C}$)	147.20		55.83	60.99	55.34	53.01
L (kJ/g)	3.15		5.16	6.43	2.67	1.77
Re-radiation (kW/m^2)	1.31		0.20	0.25	0.20	0.18

6. Conclusions

1. We are able to match the burning rate and flame characteristic of a condensed-phase fuel by matching the heat of combustion and smoke point of the condensed fuel with a gaseous fuel and inert in the BRE. This has been demonstrated for pool fires of methanol, heptane and PMMA.
2. By adjusting the fuel flow rate to match the burning rate of the pool fire with the selected gas mixture, the BRE flame yields similar burning conditions as the pool fire of 50 mm diameter, not only in the fuel property (heat of gasification), but also in the flame appearance. Although the surface temperature was not perfectly matched, the results were reasonable.
3. Extinction and ignition conditions for the burning of condensed-phase fuels can be studied much more easily and accurately with the BRE.
4. The success in validating the emulation ability of BRE burner would justify its usage in studying the burning behavior of condensed fuels of interest by using a simulation gaseous fuel. We hope to use this to explore microgravity fires.
5. Preliminary drop test results using a 50 mm BRE appears to yield nearly steady burning conditions. While these conditions may not all correspond to real condensed-phase fuels, they contribute to a flammability mapping of possible fuels that can burn.

7. Acknowledgments

The authors would like to thank M. Willnauer, E. Muller and P. Klaess for their contributions. This work was funded by NASA Grant NNX10AD98G for which Dennis Stocker is the technical contact and provided important support. Eric Neumann and his staff at NASA's Zero-Gravity Research Facility were instrumental in the successful conduct of the drop tests.

Nomenclature

B	$B \equiv \frac{Y_{ox}\Delta h_c / r - c_p(T_v - T_\infty)}{L}$
c_p	specific heat (J/kg-K)
C_f	flame standoff coefficient
d	diameter of the burner (m)
h_{vap}	heat of vaporization (kJ/g)
h_c	convective heat transfer coefficient (W/ m ² -K)
Δh_c	heat of combustion (kJ/g)
Δh_∞	heat of combustion per unit ambient oxidizer (kJ/g)
k	conductivity (W/m-K)
\dot{m}''	burning rate (g/m ² -s)
L	heat of gasification (kJ/g)
\dot{q}_e''	incident external radiative heat flux (kW/m ²)
\dot{q}_f''	incident flame heat flux (kW/m ²)
\dot{q}_{rr}''	surface radiative loss heat flux to ambient (kW/m ²)
r	stoichiometric oxygen to fuel ratio

T_s	surface temperature (°C)
T_f	flame temperature (°C)
T_v	surface vaporization temperature (°C)
T_∞	ambient temperature (°C)
Y_{ox}	ambient oxygen mass fraction

Greek

δ	flame standoff distance (m)
μ	dynamic viscosity (kg/m-s)
ρ	density (kg/m ³)
ν	kinematic viscosity (m ² -s)

References

1. Brahmi, L., Vietoris, T., Rouvreau, S., Joulain P., David L. and Torero, J.L., "Microgravity Laminar Diffusion Flame In A Perpendicular Fuel And Oxidizer Streams Configuration," AIAA J. 43: 1725-1733 (2005).
2. Bustamante, M.J., Dotson, K.T., Zhang, Y., Sunderland, P.B. and Quintiere, J.G., "Laminar Burning on Flat Wicks at Various Orientations," Spring Technical Meeting of the Central States Section of the Combustion Institute, 2012.
3. de Ris, J. and Orloff, L., "The role of buoyancy direction and radiation in turbulent diffusion flames on surfaces," Proc. Combust. Instit. 15: 175-182 (1975).
4. Kim, J.S, de Ris, J. and Kroesser, William F., "Laminar free-convective burning of fuel surfaces," Proc. Combust. Instit. 13: 949-961 (1971).
5. Li, L. and Sunderland, P.B., "An Improved Method of Smoke Point Normalization." Combust. Sci. Technol. 184: 829-841(2012).
6. Lyon, Richard E. and Quintiere, J.G. "Criteria for Piloted Ignition of Combustible Solids," Combustion and Flame 151:551-559 (2007).
7. Orloff, L. and de Ris, J., "Modeling of Ceiling Fires," Proc. Combust. Instit. 13: 979-992 (1971).
8. Quintiere, J.G., *Fundamentals of Fire Phenomena*. John Wiley & Sons Ltd., Chichester, UK, 2006.
9. Quintiere, J.G. and Rangwala, A.S., "A theory for Extinction based on Flame Temperature," Fire and Materials 28: 387-402 (2004).
10. Sunderland, P.B., Mendelson, B.J., Yuan, Z.-G. and Urban, D.L., "Shapes of Buoyant and Nonbuoyant Laminar Jet Diffusion Flames," Combustion and Flame 116: 376-386 (1999).
11. Takahashi, F. Hennigan N., and Ferkul P., Private Communications, NCSER, Cleveland, OH 44135 (2012).
12. Tewarson, A., "Generation of Heat and Chemical Compounds in Fires," *The SFPE Handbook of Fire Protection Engineering (3rd ed)*, DiNenno P.J. (ed.), National Fire Protection Association, Quincy, MA 02269, 2002, p.3-82.